



HAL
open science

The nature and partitioning of invisible gold in the pyrite-fluid system

Gleb S. Pokrovski, Maria M. Kokh, Olivier Proux, Jean-Louis F Hazemann, Elena Bazarkina, Denis Testemale, Céline Escoda, Marie-Christine Boiron, Marc Blanchard, Thierry Aigouy, et al.

► To cite this version:

Gleb S. Pokrovski, Maria M. Kokh, Olivier Proux, Jean-Louis F Hazemann, Elena Bazarkina, et al.. The nature and partitioning of invisible gold in the pyrite-fluid system. *Ore Geology Reviews*, 2019, 109, pp.545-563. 10.1016/j.oregeorev.2019.04.024 . hal-02175624

HAL Id: hal-02175624

<https://hal.science/hal-02175624>

Submitted on 22 Oct 2021

HAL is a multi-disciplinary open access archive for the deposit and dissemination of scientific research documents, whether they are published or not. The documents may come from teaching and research institutions in France or abroad, or from public or private research centers.

L'archive ouverte pluridisciplinaire **HAL**, est destinée au dépôt et à la diffusion de documents scientifiques de niveau recherche, publiés ou non, émanant des établissements d'enseignement et de recherche français ou étrangers, des laboratoires publics ou privés.



Distributed under a Creative Commons Attribution - NonCommercial 4.0 International License

1
2
3
4
5
6
7
8
9
10
11
12
13
14
15
16
17
18
19
20
21
22
23
24
25
26
27
28
29
30

The nature and partitioning of invisible gold in the pyrite-fluid system

Gleb S. Pokrovski^{1*}, Maria A. Kokh¹, Olivier Proux², Jean-Louis Hazemann³, Elena F. Bazarkina³, Denis Testemale³, Céline Escoda^{1,4}, Marie-Christine Boiron⁵, Marc Blanchard¹, Thierry Aigouy¹, Sophie Gouy¹, Philippe de Parseval¹, Michel Thibaut¹

¹ Groupe Métallogénie Expérimentale, Géosciences Environnement Toulouse (GET), UMR 5563, Observatoire Midi-Pyrénées, Université de Toulouse, Centre National de la Recherche Scientifique (CNRS), Institut de Recherche pour le Développement (IRD), 14 avenue Edouard Belin, F-31400 Toulouse, France

² Observatoire des Sciences de l'Univers de Grenoble (OSUG), UMS 832 CNRS - Université Grenoble Alpes, 414 rue de la Piscine, F-38400 Saint Martin d'Hères, France

³ Univ. Grenoble Alpes, CNRS, Institut Néel, 25 avenue des Martyrs, F-38042 Grenoble Cedex 9, France

⁴ Ecole Normale Supérieure Géologie, ENSG, 2 rue du Doyen Marcel Roubault, BP 10162, F-54505 Vandœuvre-lès-Nancy cedex, Nancy, France

⁵ GeoRessources, Université de Lorraine, CNRS, BP 239, F-54506 Vandoeuvre-lès-Nancy, France

* Corresponding author: phone: (33)-(0)5-61-33-26-18; fax: (33)-(0)5-61-33-25-60; e-mails: gleb.pokrovski@get.omp.eu; glebounet@gmail.com

Revised manuscript ORGEO_2019_063 Revision 1

19 April 2019

31 **Keywords:**

32 Invisible gold; pyrite; sulfur radical ions; high-energy resolution fluorescence-detected x-ray
 33 absorption spectroscopy (HERFD-XAS); solubility; gold deposits

34

35 **Highlights:**

- 36 • Au in sulfide-sulfate solutions is complexed with HS⁻, S₃²⁻ and S₂^{•-} ions
- 37 • In As-poor systems, invisible gold in pyrite is present as Au(0) and Au(I)
- 38 • Au(I) in pyrite occurs as S-Au-S_n moieties similar to those in the fluid
- 39 • Pyrite-fluid Au(I) partition coefficient ($D_{py/fl}$) is 0.15 ± 0.07 at 450°C and 700 bar
- 40 • Au(I) uptake from fluid by pyrite is enhanced with decreasing temperature
- 41 • $D_{py/fl}$ values allow predictions of tenors of chemically bound gold in pyrite ore

42

43 **Abstract:**

44 The most characteristic feature of hydrothermal deposits of gold is its intimate association with
 45 pyrite. Microscopically visible gold occurs in pyrite ore as metal particles of >0.1 micron in size,
 46 together with so called “invisible” gold, undetectable by conventional microscopic methods. The
 47 chemical, redox and structural state of this invisible gold and the mechanisms of its incorporation
 48 into pyrite remain both inconsistent and controversial since the dawn of economic geology. To
 49 clarify these issues, we performed laboratory experiments to simulate interactions of gold-bearing
 50 sulfur-rich hydrothermal fluids with arsenic-free pyrite at temperatures from 350 to 450°C and
 51 pressures from 400 to 700 bar, typical of the formation conditions of many types of gold deposits.
 52 Gold solubility was measured in these fluids as a function of sulfur speciation and acidity. Gold
 53 redox and structural state in pyrite was characterized by high-energy resolution fluorescence-
 54 detected x-ray absorption spectroscopy (HERFD-XAS), together with more traditional analytical
 55 techniques such as scanning electron microscopy (SEM), x-ray diffraction (XRD), electron probe
 56 micro analysis (EPMA), laser ablation inductively coupled plasma mass spectrometry (LA-
 57 ICPMS), and inductively coupled plasma atomic emission spectrometry (ICP-AES). Results show
 58 that dissolved Au in sulfide-sulfate solutions forms complexes with hydrogen sulfide, and tri- and
 59 di-sulfur radical ions whose amounts depend mostly on the fluid pH and total sulfur concentration.
 60 Invisible gold in pyrite occurs as Au metal submicron- to nano-sized particles and chemically
 61 bound Au(I) in the form of (poly)sulfide clusters composed on S-Au-S linear units, similar to
 62 those in aqueous complexes. Our findings contest the common belief that Au(I) substitutes for Fe
 63 and/or S in the structure of As-poor pyrite. The partition coefficient of Au(I) between pyrite and
 64 the fluid, $D_{py/fl}$, is determined to be 0.15 ± 0.07 at 450°C in a wide range of Au fluid phase
 65 concentrations (10-1000 ppm), but much higher $D_{py/fl}$ values, between 10 and 50, are found at
 66 350°C. These Au partitioning trends coupled with the new data on Au molecular environment in
 67 pyrite suggest a control of Au(I) incorporation in the mineral by a chemisorption step.
 68 Extrapolated to Au contents of hydrothermal fluids of the Earth’s crust which are typically below
 69 1 ppm, our $D_{py/fl}$ values reproduce fairly well the natural Au tenors in As-poor pyrites (~0.1-1 ppm
 70 Au), which are 100 to 1000 times lower than those typically observed in arsenian pyrites and
 71 arsenopyrites (10-1000 ppm Au at As tenors of 0.01-10 wt%). Our results thus indirectly highlight
 72 a key role played by arsenic in gold enrichment in As-bearing iron sulfide ore, a role that yet
 73 remains to be fully understood and quantified.

74

1. Introduction

75

76 The most characteristic feature of hydrothermal deposits of gold is its intimate
77 association with iron sulfide minerals, pyrite and arsenopyrite, in which Au concentrations may
78 reach 100 to 1000 ppm, i.e. almost million times the Au average crustal abundance. Gold affinity
79 for these minerals has been recognized since the first half of the 20th century (e.g., Goldschmidt,
80 1937). Both ‘visible’ native gold (i.e., optically detectable particles larger than 0.1-1 μm) in
81 physical association with pyrite, and ‘invisible’ (i.e., optically undetectable) gold, possibly
82 incorporated into the mineral structure, occur (e.g., Boyle, 1969; Cathelineau et al., 1989; Cook
83 and Chryssoulis, 1990; references therein). Invisible gold, also termed refractory gold, is not only
84 difficult to identify, but also hard to recover from ore (e.g., Yang et al., 1998; Adams, 2005;
85 Marsden and House, 2009). Such refractory gold poses problems both for accurate estimates of the
86 gold distribution and endowment of a deposit and for efficient extraction of the metal from iron
87 sulfide ore. Resolving these issues requires knowledge of the nature, distribution and mechanisms
88 of incorporation of invisible gold in pyrite, which all yet remain enigmatic. The present study was
89 designed in an attempt to better understand the gold-pyrite relationships, using a novel integrated
90 experimental, spectroscopic and modeling approach.

91

92 The literature on Au-bearing pyrite over the four last decades is full of discussions about
93 the chemical and redox state of invisible gold. Based on a variety of analytical techniques such as
94 scanning electron microscopy (SEM), high resolution transmission electron microscopy
95 (HRTEM), secondary ion mass spectrometry (SIMS), laser ablation inductively coupled plasma
96 mass spectrometry (LA-ICPMS), electron probe microanalyzer (EPMA), Mössbauer spectroscopy
97 (MBS), proton induced x-ray emission (PIXE), x-ray photoelectron spectrometry (XPS), x-ray
98 absorption spectroscopy (XAS), atom probe microscopy (APM), atomic force microscopy (AFM),
99 tunneling spectroscopy (STS), coupled with analyses of elemental distribution and inter-element
100 correlations, most studies agree that invisible gold occurs in two major chemical states: an
101 elemental form as nanometer-size particles of Au(0) or alloys with some other trace metals (e.g.,
102 Bi, Te, Ag), and a chemically bound form (e.g., Marion et al., 1986; Arehart et al., 1993; Scaini et
103 al., 1998; Friedl et al., 1995; Fleet and Mumin, 1997; Genkin et al., 1998; den Besten et al., 1999;
104 Simon et al., 1999; Tauson, 1999; Cabri et al., 2000; Palenik et al., 2004; Reich et al., 2005, 2006,
105 2010; Mikhlín et al., 2011; Deditius et al., 2011; Fougèrouse et al., 2016; Trigub et al., 2017).
106 However, despite significant recent advances in analytical and microscopic methods listed above,
107 the nature of this latter type of gold and factors controlling its incorporation in pyrite remain both
inconsistent and controversial. For example, the redox state of chemically bound gold varies from

108 Au³⁺ to Au¹⁺, and its coordination number from 2 to 6, according to different authors (e.g., see
109 Cabri et al., 2000 for review); such large variations make it difficult to attribute to Au an exact
110 structural position in pyrite and to identify the nature of coordinating atoms (e.g., Au, Fe, S). The
111 situation is further complicated by the presence of other minor and trace elements (Cu, Sb, Ni, Co,
112 Ag, Bi, Se, Te) and, in particular, of arsenic with which gold is systematically correlated in
113 arsenian pyrite (e.g., Reich et al., 2005). These elements, often present in far greater
114 concentrations (>0.1-1.0 wt%) than Au (typically <0.01-0.1wt%), greatly complicate the
115 assessment, using inter-element correlations, of the Au oxidation state and atomic substitutions in
116 pyrite. The use of direct redox-sensitive spectroscopic methods such as X-ray photoelectron, X-
117 ray absorption or Mössbauer spectroscopy is often limited by low concentrations, poor selectivity
118 for Au in the presence of As and other elements, and a lack of adequate standards.

119 As a result of these limitations, the mechanisms of Au incorporation in hydrothermal
120 pyrite and arsenopyrite and the role of arsenic and other elements played in this process still
121 remain hypothetical. For example, some earlier studies invoked gold transport by the fluid phase
122 in the form of Au-As-S (Sb, Se, Te) aqueous complexes and their co-precipitation with ferrous
123 iron (Boyle, 1969; Boiron et al., 1989). Other studies suggested chemisorption of dissolved Au as
124 Au-S(As) complexes at As-rich, Fe-deficient sites (Mao, 1991; Fleet and Mumin, 1997; Cepedal
125 et al., 2008), electrochemically driven adsorption of negatively charged Au(HS)₂⁻ complexes on
126 semiconducting As-pyrite and arsenopyrite surfaces (Mironov et al., 1981; Moller and Kersten,
127 1994; Widler and Seward, 2002), or Au³⁺ and Au⁺ precipitation on sulfide surfaces due to Au
128 reduction (Bancroft and Hyland, 1990; Scaini et al., 1998, Maddox et al., 1998; Mikhlin et al.,
129 2011). However, these hypotheses are mostly based on low-temperature experiments (<100°C),
130 some of them involving Au aqueous complexes (AuCl₄⁻, Au(CN)₂Br₂³⁻), which are unlikely at
131 hydrothermal conditions (e.g., see Pokrovski et al., 2014 for a review of Au speciation in
132 hydrothermal fluids). These limitations complicate the extrapolation of the results of such
133 experiments to the far greater temperatures of Au-bearing pyrite formation in nature (>150-
134 200°C). Different isomorphic substitution models of Au in the pyrite structure were also proposed,
135 including coupled substitutions of As³⁺ + Au⁺ for 2 Fe²⁺, As³⁺ + Au³⁺ for 3 Fe²⁺ (Deditius et al.,
136 2008), Cu⁺ + Au³⁺ for 2 Fe²⁺ (Chouinard et al., 2005), or Au⁺ + S²⁻ for Fe²⁺ + HS⁻ (Tauson, 1999),
137 but analytical methods capable of unambiguously supporting these models are lacking. Note that
138 the geometry of the available structural sites in pyrite composed of Fe(S₆) octahedrons and
139 S(Fe₃S) distorted tetrahedrons (Le Pape et al., 2018) is not favorable for an energetically stable
140 incorporation of both Au⁺ and Au³⁺ ions that have linear and square planar coordination
141 geometries in most inorganic and organometallic compounds (e.g., Cotton and Wilkinson, 1988).

142 Furthermore, common precipitation mechanisms of As and Au due to fluid reduction and/or
143 cooling, or coupled As-Au redox reactions on the pre-existing (arseno)pyrite have also been
144 considered (e.g., Heinrich and Eadington, 1986; Pokrovski et al., 2002), but they remain
145 qualitative owing to the complexity of the fluid composition and evolution in hydrothermal
146 systems and the interplay of multiple factors controlling mineral solubility such as temperature
147 (T), pressure (P), redox, acidity (pH), and fluid composition (Pokrovski et al., 2014).

148 It follows from this brief overview that a deeper understanding of the gold-pyrite(-
149 arsenic) relationships in hydrothermal systems awaits experimental studies at pertinent laboratory-
150 controlled conditions, coupled with Au-selective in situ spectroscopic techniques. In the recent
151 years, advances in synchrotron-based high-resolution X-ray absorption/fluorescence spectroscopy
152 (e.g., Proux et al., 2017; Manceau et al., 2018; Le Pape et al., 2018; references therein) have
153 provided an unprecedented gain both in sensitivity (metal detection limits <1 ppm) and selectivity
154 (ability to isolate the trace metal fluorescence signal in a complex mineral/organic matrix), now
155 enabling to directly “see” invisible gold in iron sulfide minerals. In this study, we designed
156 hydrothermal experiments aimed at investigating the Au-pyrite interactions in model S-bearing
157 fluid-pyrite systems at temperatures (350-450°C) and pressures (400-700 bar) typical of those of
158 various types of gold deposits, as a function of gold and sulfur speciation in the fluid phase. The
159 Au-bearing pyrites resulting from such experiments were investigated by high-resolution X-ray
160 absorption spectroscopy (HR-XAS) coupled with more “traditional” methods (EPMA, SEM,
161 XRD, LA-ICPMS, ICP-AES) to reveal the state of invisible gold in pyrite and to derive pyrite-
162 fluid partition coefficients for chemically bound Au. The results allow predictions of invisible Au
163 contents in ore, and more reliable identification of the factors leading to Au enrichment in iron
164 sulfide minerals. Although the present work deals with As-free systems, the results also help
165 indirectly assess the role of arsenic, thus providing the foundation for future experimental and
166 analytical studies on far more complex As-bearing systems.

167

168

2. Materials and methods

169

2.1. *Experimental strategy and conditions*

171

172 The primary goal of this exploratory experimental study was to investigate the state of gold
173 incorporated into pyrite under conditions pertinent to natural hydrothermal systems forming gold
174 deposits. Gold incorporation in pyrite is expected to occur via *i*) exchange of an Au-bearing

175 aqueous fluid with already existing sulfide minerals, and/or *ii*) simultaneous precipitation of gold
176 and pyrite (and other metals) from an aqueous fluid, driven by changes in T , P or fluid
177 composition. Such fluid-mineral interactions are very difficult to track from the observation of
178 complex natural mineral assemblages; alternatively, they may be simulated experimentally in
179 simplified but well-controlled systems. In this study, we designed two types of experiments to
180 reproduce the two major types of expected Au-pyrite interactions, fluid-mineral exchange and co-
181 precipitation.

182 Most previous laboratory syntheses of Au-bearing (arseno)pyrite were performed either in
183 dry (salt-flux method) or water-bearing systems at temperatures above 450-500°C from mixtures
184 of native elements with no control of redox potential, pH, and sulfur speciation, or from pre-
185 existing pyrite and fluid with excess of native sulfur leading to extremely acidic solutions (e.g.,
186 Fleet and Mumin, 1997; Tauson, 1999; Trigub et al., 2017). Such conditions are rather far from
187 those encountered in natural Au-forming hydrothermal systems, which are characterized by
188 moderate temperatures ($\leq 450^\circ\text{C}$), and near-neutral pH and redox environments allowing
189 coexistence of sulfate and sulfide in the fluid phase (Pokrovski et al., 2014; 2015). Thus, in
190 contrast to those works, our experiments were conducted in S-bearing gold-saturated fluids at
191 temperatures 350-450°C and pressures 400-700 bar, and in the presence of sulfide and sulfate over
192 a pH range 4 to 8. Our experiments allow accurate control on the concentration and speciation of
193 Au and S in the fluid phase, enabling to link, for the first time, both Au status and degree of
194 partitioning in pyrite to the fluid composition and Au aqueous speciation. A scheme summarizing
195 the experimental conditions and major steps is given in Fig. 1.

196 The run temperatures were chosen to be in the upper range of the common temperature
197 window of most Au-bearing pyrite deposits (150-500°C) to facilitate mineral-fluid exchange and
198 attainment of equilibrium within the short-time laboratory scale. Aqueous solutions of potassium
199 thiosulfate ($\text{K}_2\text{S}_2\text{O}_3$) with HCl or KOH to adjust the pH were used in both types of experiments. In
200 aqueous solution above 200°C, thiosulfate breaks down within hours to sulfate ($\text{HSO}_4^-/\text{SO}_4^{2-}$) and
201 sulfide ($\text{H}_2\text{S}/\text{HS}^-$) as the dominant sulfur species with variable amounts of the radical sulfur ions
202 ($\text{S}_3^{\cdot-}$ and $\text{S}_2^{\cdot-}$) and molecular sulfur (S_n^0), whose fractions depend on pH, temperature and S total
203 amount. Their concentrations can be predicted using the thermodynamic properties derived from
204 in-situ Raman spectroscopy data on similar thiosulfate solutions (Pokrovski and Dubessy, 2015).
205 Importantly, our S-bearing systems enable both f_{O_2} and pH buffering via sulfide-sulfate and
206 sulfate-hydrogen sulfate equilibria (Jacquemet et al., 2014), which is essential for interpretation of
207 gold solubility and speciation and can be quantified using thermodynamic modeling (section 2.8).
208 The choice of elevated S concentrations in this study (1-6 wt% total S), as compared to most

209 natural systems, was dictated by the necessity to solubilize sufficient amount of gold into the fluid
210 to favor fluid-mineral exchange and Au incorporation into pyrite in concentrations sufficient to be
211 analyzable by the methods chosen, and in particular by HR-XAS. Our experimental conditions
212 enable an accurate control on equilibrium and robust extrapolations of the obtained structural and
213 partitioning data to natural systems. Metallic gold was used as the Au source in all experiments.
214 Gold solubility in such S-rich solutions was shown to be controlled by hydrogensulfide (HS^-) and
215 trisulfur ion (S_3^{2-}) complexes, depending on pH and S concentration (Pokrovski et al., 2015). Thus,
216 the present experiments not only provide an opportunity to verify these and other alternative Au
217 speciation models in a wide pH range, but also they enable, for the first time, the exploration of
218 the impact of changes in aqueous speciation of sulfur and gold on Au incorporation in pyrite.

219

220 *2.2. Gold bearing fluid-pyrite exchange experiments*

221

222 Pyrite-fluid exchange experiments were conducted at 450°C and 700 bar in batch Ti-
223 based alloy reactors of ~20 mL volume (Fig. 1). Details about the reactor design and handling are
224 given in Pokrovski et al. (2002). The reactor was loaded with a weighed amount of aqueous ~0.5
225 mol/kg (m) $\text{K}_2\text{S}_2\text{O}_3$ (-HCl-NaOH) solution. A weighed piece of gold foil (Heraeus, 99.99% purity)
226 was attached to a titanium container suspended in the upper part of the reactor. A weighed amount
227 of iron(II) disulfide (FeS_2 , pyrite, powder, 325 mesh, 99.8% trace metals basis, <10 ppm As,
228 Sigma-Aldrich) or iron(II) monosulfide (FeS , powder, 100 mesh, 99.9% trace metals basis, <0.1
229 ppm As, Sigma-Aldrich) was placed into the container, avoiding direct contact with the gold foil.
230 The runs starting with FeS_2 and FeS are named 'Py' (for pyrite) and 'Po' (for pyrrhotite),
231 respectively (Table 1). Before experiments, the solids were characterized by XRD and SEM and,
232 after total digestion in aqua-regia, by ICP-AES (see below); they and were found to be free of gold
233 (<0.01 ppm) and contain only minor (<0.1 wt%) impurities of BaSO_4 (in FeS_2), and of FeS_2 and
234 native Fe and S (in FeS). The reactors were placed in a temperature-controlled oven ($\pm 1^\circ\text{C}$); the
235 pressure at the run temperature was estimated from the degree of filling of the reactor (which is
236 equivalent of the fluid density at experimental P - T), and using the P - T - X -density properties of the
237 well-known NaCl- H_2O system (Driesner and Heinrich, 2007) and assuming that the density of a
238 $\text{K}_2\text{S}_2\text{O}_3$ (-HCl-KOH)-bearing supercritical fluid is similar to that of an NaCl fluid of the same mass
239 concentration (wt%); this approximation induces an error of less than ± 100 bar at 450°C and 700
240 bar (e.g., Pokrovski et al., 2009a).

241 The run duration was 24 days (except 19 days for Py3 run), which was considered long
242 enough to attain the solid-fluid chemical equilibrium as shown by numerous previous experiments

243 on Au solubility in S-rich systems over a wide T range (250-450°C, Pokrovski et al., 2009a, 2015)
244 as well as by studies of Fe/Ni sulfide recrystallization in the presence of aqueous fluids at
245 temperatures as low as 120°C (e.g., Xia et al., 2009) that demonstrated attainment of equilibrium
246 within a period of a few hours to a few days. At the end of the experiment, the reactor was placed
247 in water for cooling, resulting in a fast separation of the container with the pyrite phase from the
248 fluid that condenses into liquid in the lower part of the reactor thus avoiding fluid-solid back
249 reactions, then cooled for 20 min, unloaded, and washed 3 times with hot aqua regia to remove all
250 gold that was dissolved in the fluid at the run temperature but (partly) precipitated on reactor walls
251 upon cooling. The resulting washout solution was treated and analyzed for Au (section 2.4). The
252 solid phase was rinsed with water to remove traces of salt, dried at 50°C, and analyzed as
253 described below (sections 2.5 and 2.6). The gold foil was also rinsed with water, dried, and
254 weighed to determine weight loss due to gold dissolution in the fluid and incorporation in pyrite,
255 thus providing an additional control on Au total dissolved concentrations.

256

257 2.3. Gold-pyrite co-precipitation experiments

258

259 Gold-pyrite co-precipitation was simulated at 350°C/400 bar (runs Copy1 and 2) and at
260 450°C/700 bar (run Copy3, Table 2) using a hydrothermal reactor (Fig. 1) equipped with an ultra-
261 fast sampling device and a flexible inner gold cell (150-180 cm³), adapted to multicomponent S-
262 rich systems similar to those of the present study (Pokrovski et al., 2008; Kokh et al., 2017). The
263 reactor is placed in a rocking furnace and the temperature ($\pm 1^\circ\text{C}$) and pressure (± 5 bar) are
264 controlled independently during the run. The reactor is equipped with a sampling tube, two high-
265 pressure titanium valves and a titanium vial tightly assembled to the second valve; this design
266 allows for almost instantaneous (within < 1 s) sampling of a portion of the fluid phase pushed by
267 the internal pressure from the reactor, thus avoiding any solute precipitation or degassing, which
268 would have inevitably occurred in S-rich systems using traditional sampling procedures. The cell
269 was loaded with an aqueous thiosulfate solution and the reactor was brought to the desired P - T ;
270 the fluid was periodically sampled to monitor attainment of gold solubility equilibrium, and
271 processed and analyzed as described below (section 2.4). The composition of the fluid may be
272 modified in situ at high P - T during the run via injection, using a calibrated capstan pump, of a
273 given amount of another solution (e.g., HCl in CoPy3 experiment) inducing controlled changes in
274 pH and Au solubility. Furthermore, in the final step of the three CoPy experiments, an FeCl₂
275 solution was injected into the cell, inducing pyrite precipitation followed by re-equilibration
276 between the precipitated pyrite and the fluid of modified composition. At the run termination, the

277 reactor was cooled down within a few hours and the pyrite precipitate was recovered. Compared
278 to the batch reactor technique (section 2.2), the flexible-cell reactor enables far more accurate,
279 time- and composition-resolved measurement of gold solubility and sulfur speciation in the fluid
280 at high P - T , but does not allow fast recovery of the solid phase that might potentially be subject to
281 some modifications (e.g., Au precipitation or re-dissolution) during the inevitably slow cooling of
282 the 80-kg reactor.

283

284 *2.4. Chemical analyses of experimental solutions*

285

286 Chemical treatment and analyses of gold, other metals and sulfur in the experimental
287 solutions were performed using protocols developed in Kokh et al. (2016, 2017). Briefly, Au
288 concentrations in aqua-regia washout solutions from experiments in batch reactors were analyzed
289 by ICP-MS and/or ICP-AES. The sample preparation recipe consists of gentle evaporation of the
290 aqueous sample on hot plate (at 60-80°C) in a clean Teflon vial (Savilex©) until a wet salt residue
291 is obtained; then reacting the residue with 2 g of hot aqua regia in the closed vial (at 120°C for ~2
292 h), followed by gentle evaporation of the solution to 0.2-0.3 g (at 60-70°C), and finally dilution of
293 the rest by ultra-pure doubly-distilled 0.5wt% HCl – 1.5wt% HNO₃ in water. Gold, K and Fe in
294 the fluids from experiments in the flexible-cell reactor were treated and analyzed using the same
295 protocol for fluids sampled into an NH₃ (28 wt% NH₃ in water) solution (Kokh et al., 2016). The
296 overall analytical uncertainties (which include sample treatment and ICP-MS or ICP-AES
297 analysis) on the final concentration do not exceed 10% of the value.

298 Chlorine and sulfur were also analyzed in fluids sampled from the flexible-cell reactor.
299 Total chloride was quantified (as the Cl⁻ ion) by high-performance liquid chromatography
300 (HPLC). Total dissolved sulfur (S_{tot}) was analyzed by ICP-AES and/or HPLC (as the SO₄²⁻ ion)
301 after complete oxidation to sulfate in NH₃-H₂O₂ solutions. Both methods for S showed an
302 agreement within 10% of the total concentration value. Total reduced sulfur (S_{red}, dominantly
303 hydrogen sulfide, and eventually sulfite and polysulfide) was quantified by iodometric titration.
304 Hydrogen sulfide (H₂S/HS⁻) was separated from the other sulfur species by precipitation as
305 cadmium sulfide (CdS) and centrifugation, followed by iodometric titration of CdS in acid
306 solution (10 wt% HCl). Sulfate was analyzed gravimetrically from the fluid sampled directly in a
307 1 m Ba acetate solution resulting in precipitation of BaSO₄, which was subsequently washed,
308 centrifuged, and dried before weighing. Uncertainties of the Cl and S analyses are less than 10%
309 of the value. The concentrations of Au and other solutes in batch and flexible-cell reactor
310 experiments are reported in Table 1 and 2, respectively.

311

312 *2.5. Conventional analyses of experimental pyrites*

313

314

315

316

317

318

319

320

321

322

323

324

The solids recovered from both types of experiment were analyzed for phase composition and major element contents by XRD, SEM and EPMA (Table 3). The analyses showed pyrite as the major phase with variable amounts of visible gold particles (0.1-10 μm) in almost all experiments, plus minor pyrrhotite (<5%) in the two batch-reactor runs started with FeS (Po1 and Po2, Table 1, Fig. 2). Total gold was quantified by dissolution of a weighed amount of the bulk pyrite solid in hot aqua-regia, followed by the same treatment as that for the aqueous solutions (Section 2.4) and ICP-AES analysis. Visible gold contents were also independently estimated on polished sections by SEM-EDS mapping of a given surface area (typically $\sim 1 \text{ mm}^2$). The surface of gold particles, being much brighter in back scattered electron (BSE) mode than pyrite (e.g., Fig. 2), was measured and compared to the surface of all pyrite grains using the ImageJ software. The visible Au concentration (in ppm) was then estimated as:

325

$$C_{Au(0)}(\text{ppm}) = (S_{Au(0)} \times \rho_{Au} \times 10^6) / (S_{Pyrite} \times \rho_{Pyrite}) \quad (1)$$

326

327

328

329

330

where $S_{Au(0)}$ and S_{Pyrite} are the surfaces of gold and pyrite grains respectively, and $\rho_{Au(0)}$ and ρ_{Pyrite} are the densities of pure metallic gold (19.3 g/cm^3) and pyrite (5.0 g/cm^3), respectively. Although these analyses are subject to large uncertainties due to the potentially limited representativeness of the examined polished surfaces and SEM resolution, they nevertheless provide a useful estimate of visible gold content for Au-rich samples (>0.1 wt% total Au).

331

332

333

334

335

336

337

338

An attempt was also made to analyze invisible Au in large pyrite crystals (>10 μm), by carefully avoiding visible Au particles, using EPMA (Cameca SX Five microprobe, electron beam spot $\sim 1 \mu\text{m}$, accelerating voltage 25 kV, current 100 nA, counting time 240 s). All analyses for the fluid-pyrite exchange runs (Py and Po series) were, however, only a factor of ~ 2 above the EPMA detection limit of $\sim 120 \text{ ppm Au}$, in agreement with low invisible gold concentrations found by X-ray absorption spectroscopy in these samples, whereas the co-precipitation runs (CoPy series) yielded much higher Au contents (1000s ppm), which match the XAS-determined concentrations within a factor of 2 (section 2.6).

339

340

341

342

343

Selected samples were also analyzed for Au by LA-ICPMS using a Finnigan MAT Element equipped with a femtosecond UV laser (laser spot diameter $\sim 20 \mu\text{m}$ yielding an ablation crater of 25-30 μm , energy 0.003 mJ, fluency 0.94 J/cm^2 , power 12%, frequency 5 Hz, background time 45 s, ablation time 60 s). Transient ablation signals were converted to concentration using the SILLS software (Guillong et al., 2008), and an external Au-bearing FeS

344 standard (LaFlamme Po726 standard reference material, 46 ± 2 ppm Au, Sylvester et al., 2005) and
345 Fe content in pyrite as the internal standard. Although the LA-ICPMS technique offers much
346 higher sensitivity compared to EPMA, with typical detection limits of 0.1 ppm Au for our
347 samples, the major challenge of such analyses is the small pyrite grain size being typically <10-40
348 μm with rare exceptions (Fig. 2), which is smaller than or comparable to the ablation spot size. In
349 addition, the LA-ICPMS analysis is much more penetrative than EPMA, with ablation depth
350 superior to the beam spot diameter (>20 μm). As a result, these analyses of individual pyrite grains
351 (by avoiding “visible” >1 μm gold particles, where possible), allow only a rough estimate of total
352 invisible gold content, and provide information about Au distribution across the grain depth. This
353 analysis cannot exclude the presence of gold nuggets inside or underneath a pyrite grain. An
354 attempt to reduce the laser spot to 5 μm allowed elimination of some of the largest spikes, but
355 yielded too unstable and weak ablation signals to obtain accurate analytical results for our
356 particular samples. Recent developments of LA-ICPMS time-of-flight set-ups (e.g., Gundlach-
357 Graham et al., 2018) would enable, in near future, high-resolution quantitative elemental imaging
358 of gold and other trace metals in analytically challenging pyrite samples like those of the present
359 study.

360

361 *2.6. High-resolution X-ray absorption spectroscopy (HR-XAS) analyses of experimental pyrites*

362

363 HR-XAS analyses at the Au L₃ edge (~11.920 keV) of experimental pyrite samples were
364 performed at FAME (BM30b) beamline of the European Synchrotron Radiation Facility,
365 Grenoble, France (Proux et al., 2005), using a recently developed 5-crystal spectrometer operating
366 in high-energy resolution fluorescence detected (HERFD) mode (Llorens et al., 2012). The two
367 main advantages of using HERFD compared to traditional XAS spectroscopy are *i*) a significant
368 gain in spectral resolution compared to nominal resolution defined by the core hole width of the
369 absorption edge, allowing the detection of different features in X-ray absorption near-edge
370 structure (XANES) spectral region, which are indicative of Au redox state and coordination
371 geometry, and *ii*) the ability to efficiently filter out all unwanted contributions from elastic
372 scattering and fluorescence from other elements (e.g., As whose absorption edge is within 50 eV
373 of that of Au) in the sample and thus significantly improve both the limit of detection for Au and
374 signal-to-noise ratio of XAS spectra. In addition, L₃-edge XANES spectra at nominal resolution of
375 most Au(I) compounds and complexes with common ligands (S, Cl, P) are quite similar and rather
376 featureless (Fig. 3; Pokrovski et al., 2009a,b, 2015), making it difficult to unambiguously

377 distinguish between the different Au coordination environments and the identity of neighboring
378 atoms.

379 The beamline X-ray optics incorporated a Si(220) double crystal monochromator with
380 sagittal focusing providing a beam spot (full width at half maximum) of $\sim 200 \times 300 \mu\text{m}^2$ at the
381 sample, Rh-coated mirrors for harmonic rejection, and a crystal analyzer spectrometer (Llorens et
382 al., 2012) with five Si(660) crystals placed in a Roland circle geometry (Bragg angle = 85.71°).
383 This device allows a resolution of $1.3 \pm 0.1 \text{ eV}$ at the $L\alpha$ Au fluorescence line measured as full
384 width middle height (FWMH) of the elastic peak, providing a gain in resolution by a factor of ~ 5
385 compared to nominal spectral resolution (natural core-hole width is 5.4 eV at the Au L_3 -edge).
386 High-resolution fluorescence XANES (hereafter HR-XANES) spectra were recorded using a
387 Vortex EX-90 mono-element detector. In addition, nominal-resolution transmission spectra were
388 acquired at the same time as HERFD spectra for all samples and reference compounds. The pyrite
389 samples from hydrothermal experiments were homogenized by mild grinding, which was
390 necessary for obtaining XAS signals devoid of harmonics, diffraction peaks, spectral distortions,
391 and self-absorption artifacts which are all common for inhomogeneous samples (e.g., Curis et al.,
392 2005; references therein). The produced powders were pressed in 5-mm diameter pellets, affixed
393 with silicon grease to a copper holder and placed in a liquid He cryostat ($\sim 10 \text{ K}$) to reduce X-ray
394 beam-induced damage common for redox-sensitive elements like Au (Pokrovski et al., 2009b). A
395 helium-filled bag was placed to fill the space between the crystal analyzers, cryostat window
396 where the pyrite sample is placed, and detector, to reduce the absorption of the Au fluorescence
397 signal by air. Different reference Au-bearing compounds (Au, Au_2S , $\text{Na}_3\text{Au}(\text{S}_2\text{O}_3) \times 1-2\text{H}_2\text{O}$,
398 AuAgS , Au-thiomalate, $\text{K}_2\text{AuCl}_4 \times 1-2\text{H}_2\text{O}$, AuTe_2 , Au-doped CuS, AuSb_2 , $\text{AuClP}(\text{Phen})_3$ and
399 $\text{AuCl}(\text{P}(\text{Phen})_3)_2$ where Phen is the phenol cycle $\text{C}_6\text{H}_5\text{OH}$) were diluted by mixing with boron
400 nitride powder to obtain an Au concentration of 1 to 2 wt%, comfortable for fluorescence
401 measurements but low enough to avoid self-absorption effects that lead to damping of XANES
402 amplitudes. The prepared powders were pressed in pellets and recorded similarly to the pyrite
403 samples, both in transmission (nominal resolution) and fluorescence (high-resolution) modes.

404 Since our pyrites contain both visible and invisible gold (Fig. 2), care was taken to avoid
405 gold particles larger than $\sim 1 \mu\text{m}$ and to assure relative homogeneity of Au concentrations over the
406 whole beam size during the acquisition, which is essential for obtaining accurate and reproducible
407 XAS spectra. The acquisition spots were thus carefully chosen by scanning the pellets in two
408 directions (e.g., Fig. A1). The X-ray beam was positioned sufficiently far from large fluorescence
409 peaks arising from gold particles to allow us to probe essentially invisible and relatively
410 homogeneously distributed gold in the sample. For most pyrite samples of low Au concentration

411 (<100 ppm) multiple scans (5 to 20) were recorded and, if found similar, merged together to
 412 increase the signal-to-noise ratio. The concentration of invisible gold in pyrite in the acquisition
 413 spots may directly be determined from the edge height of the fluorescence spectrum using a
 414 standard of known Au concentration with similar matrix major elements (Fe, S), measured at
 415 identical acquisition conditions. The standard used in this study is a mixture of natural Au-bearing
 416 pyrite and arsenopyrite from the Villeranges deposit, France (sample MCB-7358) in which gold is
 417 present exclusively in a chemically bound state as demonstrated by Mössbauer spectroscopy
 418 (Boiron et al., 1989). Total concentrations of Fe, S, As and Au in the standard were determined by
 419 ICP-AES after complete aqua-regia digestion of the solid. The obtained solid composition
 420 corresponds to the formula $\text{FeAs}_{0.28}\text{S}_{1.72}$ with 450 ± 50 ppm Au. The solid was ground, pressed in a
 421 pellet, and measured by XAS similarly to the experimental pyrite samples (detailed account of Au
 422 XAS spectra of this and other natural and synthetic arsenian pyrites and arsenopyrites will be
 423 given elsewhere). Gold concentrations in our pyrite samples were thus determined using
 424 proportionality between absorption edge height in fluorescence mode ($\Delta\mu_{\text{fl}}$) and Au concentration
 425 for a pyrite sample (*Py*) and the standard (*St*):

$$426 \quad C_{\text{Au}}(\text{Py}) = \Delta\mu_{\text{fl}}(\text{Py}) \times C_{\text{Au}}(\text{St}) / \Delta\mu_{\text{fl}}(\text{St}) \quad (2)$$

427 HR-XANES spectra were normalized to the absorption edge height with the Athena
 428 software (Ravel and Newville, 2005) to compare with spectra of reference compounds and
 429 perform linear combination fits (LCF) to quantify the contributions from different Au structural
 430 environments and to directly distinguish between native and chemically bound gold. Furthermore,
 431 the experimental XANES spectra were compared with quantum-chemically simulated ones for
 432 different Au cluster geometries and substitution models in pyrite. Due to relatively low Au
 433 concentrations, the insufficient signal-to-noise ratio of most pyrite samples did not allow
 434 acquisition of extended x-ray absorption fine structure (EXAFS) spectra good enough to extract
 435 accurate structural information. Most EXAFS spectra had low signal-to-noise ratios and short
 436 exploitable energy ranges ($3 < k < 8 \text{ \AA}^{-1}$, where *k* is photoelectron wavenumber), which resulted in
 437 large errors on Au nearest coordination numbers ($2 < N < 6$ atoms) and interatomic distances
 438 ($2.2 < R < 2.4 \text{ \AA}$). As a result, in this study we rely on the analyses of the HR-XANES experimental
 439 and quantum-chemistry simulated spectra.

440

441 2.7. Quantum-chemistry ab-initio modeling of XANES spectra using FDMNES

442

443 Direct and unambiguous interpretation of XANES spectra, particularly in high-resolution
 444 mode, requires reference compounds with Au redox and structural environments closely matching

445 those of the samples. Since no such stable compounds with known structures exist in the Au-Fe-
446 S(-As) system, a theoretical simulation of XANES spectra for expected Au geometries and
447 structures in pyrite is the only alternative. Such simulations become now possible due to
448 significant progress in quantum-chemical modelling of full electron potential in the near-edge
449 absorption region, coupled with increasing computer power enabling the use of Fine Difference
450 Methods (FDM) for solving the Schrödinger equation on the node points of a three-dimensional
451 grid (Amestoy et al., 2006; Guda et al., 2015). We used the FDMNES code (Joly, 2001; Bunau and
452 Joly, 2009) to calculate theoretical Au L₃-edge XANES spectra of different possible Au local
453 structures and geometries in pyrite (e.g., Au substitution in the Fe or S structural sites, different
454 Au-S_n clusters similar to those in aqueous solution adsorbed on pyrite surface) and to compare
455 them with the experimental spectra. All calculations were performed in FDM mode (note that in
456 case of low symmetry, the muffin-tin approximation is not sufficient in the near-edge energy
457 range; Joly, 2001; Testemale et al., 2004), and accounting for relativistic effects and spin-orbit
458 interactions intrinsic to heavy atoms such as gold (program's keywords 'Relativism' and
459 'Spinorbit'; Joly, 2018). The obtained raw calculations represent the evolution of the photo-
460 absorption cross-section of Au as a function of X-ray photon energy and correspond to the
461 transition amplitude between the initial and final states with an energy resolution of the FD method
462 (<0.1 eV). These spectra, which display almost all possible electronic transitions, are further
463 convoluted with a Lorentzian function (keyword 'Arc') with a width of 1.3 eV (keyword
464 'Gamma_hole'), which corresponds to the energy resolution of our HERFD setting (section 2.6).

465

466 *2.8. Thermodynamic calculations in experimental fluid-mineral systems*

467

468 Gold and sulfur speciation and solubility in the fluid phase of the experimental systems
469 were modelled using available robust thermodynamic data, and the results were compared with the
470 measured Au solubility. Calculations were performed using the HCh software package and
471 associated Unitherm database, allowing chemical equilibrium simulations in multicomponent
472 fluid-mineral systems based on the minimization of the Gibbs energy of the system (Shvarov,
473 2008; 2015), and accounting for non-ideality of the fluid using the extended Debye-Hückel
474 equation (Helgeson et al., 1981). The selection of thermodynamic data sources was discussed in
475 detail elsewhere (Pokrovski et al., 2015; Kokh et al., 2017), and will only briefly be summarized
476 here.

477

478 The thermodynamic properties of the minerals, major fluid components, and most sulfur
aqueous species were taken from the updated SUPCRT (Johnson et al., 1992), JANAF (Chase,

479 1998), and Robie and Hemingway (1995) databases, complemented by recent data for ionic sulfur
480 forms including S_3^- (Pokrovski and Dubessy, 2015; references therein) using the revised and
481 extended HKF (Helgeson-Kirkham-Flowers) equation of state (Oelkers et al., 2009; Sverjensky et
482 al., 2014; references therein). The thermodynamic properties of the molecular sulfur aqueous
483 forms, H_2S , SO_2 and H_2 and O_2 , were adopted according to a recent model for aqueous non-
484 electrolytes (Akinfiyev and Diamond, 2003), which allows a more accurate description over the P - T
485 range relevant to our study (350-450°C; <1 kbar) than the SUPCRT database, which used a more
486 limited experimental dataset in derivation of the HKF model coefficients for these species.
487 Noteworthy, the thermodynamic data from Akinfiyev and Diamond (2003) were also used in
488 derivation of the thermodynamic properties of Au species (see below), and thus were chosen here
489 to maintain thermodynamic consistency.

490 The thermodynamic properties of the Au^+ cation, and its traditional hydrogen sulfide
491 ($AuHS$, $Au(HS)_2^-$) and hydroxide ($AuOH$) species were taken from a recent compilation of
492 Pokrovski et al. (2014), consistent with most recent experimental data. The Gibbs energy value of
493 the di-chloride species ($AuCl_2^-$) for which there is a more substantial disagreement among the
494 major data sources, was taken as an average between those reported in Pokrovski et al. (2014) and
495 Stefansson and Seward (2003). Species such as $AuCl$ and $Au(OH)_2^-$, tentatively suggested in some
496 previous compilations, were ignored in the present modeling both because their existence in
497 hydrothermal solutions is not explicitly proven by direct experimental data and their parameters
498 are based on estimations at ambient conditions and thus are subject to large errors at elevated
499 temperatures. Among the traditional species, only $Au(HS)_2^-$ was found to significantly contribute
500 to the measured Au solubility in our S-rich systems at near neutral pH. The recently discovered
501 gold complex with the trisulfur ion, $Au(HS)S_3^-$ (Pokrovski et al., 2015), accounting for Au
502 solubility in acidic-to-neutral solutions, was also included in the model. In addition, a tentative Au
503 complex with the disulfur radical ion, S_2^- , which has been detected by in-situ Raman spectroscopy
504 in similar thiosulfate aqueous solutions (Pokrovski and Dubessy, 2015), was also tested to account
505 for the measured solubility (section 4.1). It should be emphasized that our choice of
506 thermodynamic data sources for major sulfur forms and its complexes with gold is self-consistent,
507 which is a key condition for accurate interpretation of Au speciation and solubility in S-rich
508 systems at elevated temperatures, similar to those of the present study (e.g., Pokrovski et al.,
509 2015).

510

511

3. Results

512 *3.1. Gold concentration in the fluid phase*

513

514 *3.1.1. Batch-reactor experiments*

515 Gold concentrations measured in quenched solutions from batch-reactor experiments at
516 450°C and 700 bar are reported in Table 1. The dissolved Au concentrations vary from ~100 ppm
517 (in acidic solutions) to almost 3000 ppm (in alkaline solutions). A reasonable quantification limit
518 for aqueous Au in our experimental systems is about 100-150 ppm, which is due to intrinsic
519 uncertainties of the batch-reactor technique such as incomplete recovery of Au precipitated on the
520 reactor walls after the quench, possible recrystallization of Au in the reactor during the run due to
521 minor temperature gradients, mechanical detachment of gold metal particles from the foil
522 suspended in the upper part of the reactor, and uncontrolled gold dissolution during the reactor
523 heating or cooling. These artifacts may result either in overestimation or underestimation of the
524 true gold solubility (see section 4.1). Total gold dissolved concentrations can independently be
525 estimated from weight loss of the gold foil after the experiment (with a reasonable detection limit
526 of ~50 ppm Au and an uncertainty of ± 50 ppm Au corresponding to weight loss of <0.5 mg). This
527 estimation takes into account Au incorporation in pyrite, but is obviously subject to the same
528 artifacts. It can be seen in Table 1 that for the runs with low Au solubility in the fluid producing
529 Au-poor pyrites (Py1, 3 and 6) the gold weight-loss derived concentrations are similar within
530 errors to those derived from quench-solution analysis. For runs in the presence of initial pyrite and
531 with higher Au aqueous concentrations and less acidic pH (>400 ppm Au, Py2, 4 and 5), the
532 weight-loss derived concentrations are also in agreement with those from the quenched solution,
533 demonstrating almost complete recovery of gold and a negligibly small (within the associated
534 errors) fraction of the Au incorporated in pyrite. By contrast, runs starting with FeS (Po1, 2)
535 yielded significantly higher loss-weight Au concentrations compared to those derived from
536 quenched solution, demonstrating that a more important fraction of Au was precipitated on and/or
537 incorporated into the solid phase during FeS transformation into pyrite, as also confirmed by direct
538 analyses of the solid phase (section 3.2).

539

540 *3.1.2. Flexible-cell reactor experiments*

541 Gold and other solute (S, Cl, K, Fe) concentrations, measured in sampled portions of fluid
542 as a function of time in co-precipitation experiments conducted at 350 and 450°C using the
543 flexible-cell reactor (Copy1, 2 and 3), are reported in Table 2. It should be emphasized that these
544 direct measurements are not subjected to the artifacts common for the batch-reactor method
545 enumerated above and thus may be considered to represent the true gold solubility values. The

546 uncertainties of Au solubility are less than 10% of the total value; they stem mostly from the S-
547 rich solutions treatment and analysis by independent methods (ICP-MS, ICP-AES). It can be seen
548 that Au dissolved concentrations before pyrite precipitation were constant within errors for run
549 durations from 1 to 10 days, demonstrating attainment of saturation with metallic gold. After
550 pyrite precipitation was induced by injection of FeCl₂ solutions, gold dissolved concentrations
551 dropped by a factor of 5 to 10 (depending on the experiment), in response to the large decrease of
552 aqueous S concentration upon scavenging by pyrite and the resulting breakdown of gold-sulfur
553 complexes. The Au aqueous concentrations after pyrite precipitation either increase by a small
554 factor (2 to 3) with time (e.g., CoPy1), remain stable (CoPy2), or slightly decrease (CoPy3), likely
555 reflecting the longer times for the system to recover after a large and rapid change in S
556 concentration, and the different reaction kinetics of Au-pyrite-fluid exchange and pyrite
557 recrystallization, which may depend on fluid composition, acidity, and temperature.

558 The concentrations of other fluid constituents (total S, K, Cl) are in excellent agreement
559 with the initial and injected quantities. Measured total dissolved sulfur contents (S_{tot}) are identical
560 within errors to the sum of aqueous sulfide and sulfate concentrations in CoPy2 and CoPy3,
561 suggesting that other S species concentrations (e.g., radical ions, polysulfides) are small. By
562 contrast, in more acidic CoPy1 experiment, S_{tot} concentrations are by 20 to 30% higher than the
563 sum of sulfate and sulfide, likely due to the presence of molecular sulfur in the experiment, as
564 demonstrated by in situ Raman spectroscopy on similar solutions (Pokrovski and Dubessy, 2015);
565 this form of sulfur is not analyzable in sampled fluids by the I₂, CdS and BaSO₄ protocols
566 employed in this study (section 2.4). A more detailed account of sulfur speciation and isotope
567 fractionation in these experiments will be given elsewhere.

568

569 *3.1.3. Comparison of Au solubility between the two methods*

570 The dissolved Au concentrations in the flexible-cell reactor experiment at 450°C and 700
571 bar (CoPy3, Table 2) before and after HCl injection can directly be compared with those from
572 batch-reactor runs of similar *P-T* and fluid composition (Py4 and 5; Table 1), in particular to
573 evaluate the accuracy of the batch-reactor solubility measurements. The Au concentrations
574 measured in batch reactors both in alkaline and neutral solutions (~2800 ppm Au in Py5, 0.5m
575 K₂S₂O₃-0.3m KOH; ~1600 ppm Au in Py4, 0.5m K₂S₂O₃; Table 1) are 2 to 3 times higher than the
576 flexible-cell reactor Au concentrations at similar solution compositions (~1300 ppm Au in CoPy3,
577 initial fluid with 0.5m K₂S₂O₃-0.3m KOH; ~600 ppm Au in fluid after HCl injection resulting in
578 almost complete neutralization of KOH, ~0.41m K₂S₂O₃-0.2m KCl). Such discrepancies cannot be
579 caused by minor differences in solution composition between the two types of dissolution

580 experiments or by the presence of pyrite in the batch-reactor experiments since pyrite solubility is
581 negligibly small at these conditions as shown by thermodynamic modeling ($<10^{-4}$ m Fe).
582 Therefore, the overestimated Au concentrations in the S-rich solutions in the batch-reactor
583 compared to the flexible-cell reactor experiments at 450°C are likely due to enhanced dissolution
584 of Au during the temperature rise in batch-reactor runs that largely exceeds the Au saturation
585 concentrations at 450°C. Indeed, thermodynamic predictions of gold solubility, using the stability
586 constant for the dominant $\text{Au}(\text{HS})_2^-$ complex at this pH range (see Section 2.8), show a solubility
587 maximum at 200-250°C in neutral-to-alkaline S-rich solutions, followed by a pronounced
588 solubility decrease at higher T , with Au saturation concentrations ~ 10 times lower at 450°C (Fig.
589 A2a,b). Such Au solubility pattern versus temperature in sulfide solutions is known for a long time
590 (Pokrovski et al., 2014; references therein). Considering the very fast dissolution kinetics of
591 metallic Au in such solutions over the T range 150-450°C, as was shown by time-dependent in-
592 situ XAS measurements (Pokrovski et al., 2009a), it is thus very likely that some additional Au
593 was added to the solution by dissolution between ~ 200 and $\sim 300^\circ\text{C}$ during heating of the batch
594 reactors. When reaching 450°C, such Au-rich solution became oversaturated and gold re-
595 precipitated on the reactor walls, contributing both to the washout solution and weight loss
596 analyses reported in Table 1. This artifact of the batch-reactor method, which has not been
597 recognized in previous studies that employed the same technique in S-rich (>0.5 m) neutral to
598 alkaline solutions (e.g., Trigub et al., 2017), requires corrections when interpreting Au speciation
599 and solubility.

600 Consequently, in the following discussion (section 4.1), we tentatively corrected by a
601 factor of 0.5 the measured Au concentrations in batch-reactor runs Py4 and Py5. By contrast, in
602 more acidic S-rich solutions, in which Au speciation is dominated by $\text{Au}(\text{HS})\text{S}_3^-$, gold solubility
603 only weakly depends on temperature, and thus is not expected to be overestimated in batch-reactor
604 experiments (Fig. A2c). Similarly, at lower sulfide concentrations (<0.2 m, such as in Po1 and Po2
605 runs, in which $>$ half of initial S was consumed by pyrite formation), the amplitude of Au solubility
606 decrease from 250 to 450°C is much smaller and thus may be neglected. The Au aqueous
607 concentrations adopted in this study are reported in Table 4 and used for interpreting Au aqueous
608 speciation and fluid-pyrite partitioning (sections 4.1 and 4.3).

609

610 *3.2. Gold state and concentration in pyrite from conventional analyses*

611

612 The complementary analytical methods employed in this study help distinguish the
613 different states of gold associated with pyrite and estimate their approximate concentrations in the

614 solid phase (Table 3). Visible gold contents in pyrites from exchange experiments determined by
615 SEM mapping are highly variable, ranging from ~100 ppm for runs starting with pyrite (Py1 to 5)
616 to ~20,000 ppm in runs starting with FeS (Po1 and 2). The Au enrichment in the Po runs is due to
617 precipitation of native gold from the solution upon sulfidation of FeS to FeS₂ and scavenging of
618 part of sulfur from the fluid and the resulting decrease in gold solubility, as a result of fast gold-
619 fluid re-equilibration (section 3.1). Native gold contents estimated by SEM, despite their large
620 uncertainties (>50% of the value, section 2.2), compare reasonably well with total Au contents in
621 the solid phase determined by aqua-regia digestion followed by ICP-AES. These contents are 100s
622 ppm for Py runs and 1,000s ppm for Po runs. Furthermore, an independent estimate of the total
623 gold amount associated with pyrite in batch-reactor experiments may be made from the difference
624 between Au concentrations measured in washout solutions and those calculated from weight loss
625 of the Au foil (Table 1). For the Py runs this difference is zero within errors. In contrast, in the two
626 Po runs Au weight-loss significantly exceeds Au washout content; this difference corresponds to
627 pyrite-scavenged Au concentrations of ~10,000 ppm, fairly comparable (within 50%) with those
628 derived from SEM and total digestion analyses (Table 3).

629 An attempt to determine invisible gold contents in pyrites was made using EPMA by
630 carefully avoiding microscopic grains of native gold. These contents were found to be only
631 slightly higher (factor of <2) than the detection limit of the technique (<120 ppm Au) for all
632 pyrites from exchange experiments, and thus EPMA analyses may provide only qualitative
633 information. Nevertheless, the variation of Au concentrations among different data points acquired
634 at different positions at the grain and for different grain sizes (from 5 to ~50 μm) is rather small
635 (relative standard deviation, RSD <20%, Table 3), suggesting no significant invisible gold zoning
636 or noticeable enrichment of small grains. In contrast, pyrites from co-precipitation runs (Copy1
637 and 2) exhibit quantifiable invisible Au concentrations of 1,000s ppm on average but with
638 significant data scatter (RSD > 50%, Table 3) likely due to presence of heterogeneously
639 distributed submicron to nano particulate gold, which could be observed at highest magnification
640 in EDS images of Au-bearing precipitated pyrite (Fig. 2e, f).

641 LA-ICPMS analyses of selected samples also show a rather heterogeneous gold
642 distribution across an individual pyrite grain and between different grains in the same sample
643 (Table 3, Fig. A3). Coexistence of spiky signals and regions of relatively constant signal intensity
644 as a function of time in the same ablation measurement confirms, in agreement with the other
645 conventional methods above, the presence of different types of gold in pyrite at micron scale.
646 These include relatively large (μm size) particles of native gold, together with clusters of smaller
647 sub-micron particles, and crystal domains with more homogeneously distributed invisible gold.

648 The few spatially resolved data points that could be acquired across rare large grains (40-50 μm)
649 or on individual grains of different size (from 10 to 50 μm) do not show systematic correlations
650 with Au concentration (Fig. A3). Because of the relatively low spatial resolution of LA-ICMPS,
651 compared to SEM and EPMA, and small data statistics, no further quantification was possible for
652 our fine grain samples. Nevertheless, despite these limitations of LA-ICPMS, the mean Au
653 concentrations for each analyzed sample (Py2, Py5, Po1, and CoPy3; Table 3) match within errors
654 those of invisible gold from EPMA and XAS analyses. A more accurate assessment of the
655 different Au chemical forms and their fractions is provided by HR-XAS spectroscopy in the
656 following section.

657

658 *3.3. Gold speciation and concentration in pyrite from HR-XANES spectroscopic analyses*

659

660 HR-XANES scans were recorded on relatively “flat” regions of the pyrite pellets (i.e.,
661 those showing a constant fluorescence signal versus beam spot position, e.g., Fig. A1) by avoiding
662 large Au particles ($>1 \mu\text{m}$) clearly identifiable by their intense fluorescence signals and XANES
663 spectra similar to those of native gold references. The total invisible Au concentration, which is
664 determined using the edge step height of the fluorescence spectrum at each acquisition point
665 (equation 2), varied less than 20% of the value; its average for each sample is reported in Table 3.
666 These fluorescence-derived invisible gold concentration values are far more accurate than those
667 from the EPMA and LA-ICPMS analyses above, since the technique is sensitive enough
668 (detection limit is $<1 \text{ ppm Au}$) and more representative of the whole sample because of the much
669 larger X-ray beam size ($\sim 300 \mu\text{m}$) than the EPMA (1-3 μm) or LA-ICPMS (20-30 μm). Thus, the
670 fluorescence-derived values of invisible gold concentration were retained in the subsequent
671 interpretation (section 4).

672 Absorption edge-height normalized XANES spectra of selected pyrite samples are shown
673 in Fig. 4. There are three groups of samples differing by the dominant state of invisible Au, as
674 inferred by comparisons with the spectra of metallic gold and Au(I) and Au(III) reference
675 compounds. Some pyrites (Po1, 2; CoPy2, 3) have spectra very similar to those of elemental gold
676 demonstrating that Au(0) largely dominates in those samples. The two major distinguishing
677 features of the HR-XANES Au(0) spectrum are *i*) a relatively low-amplitude white-line with a
678 wide uneven top over 11,920-11,923 eV, and *ii*) an intense resonance centered around 11,945 eV.
679 These main features are little sensitive to gold particle size, ranging from $>1 \mu\text{m}$ down to 5 nm, as
680 shown by XANES spectra of micron-particle Au metal and a nano-particle Au suspension (Fig. 4).

681 The spectra directly confirm the large abundance of metallic gold in the first group of samples as
682 also qualitatively indicated by SEM, EMPA and LA-ICPMS (Table 3). Another group of samples
683 (Py1, 2, 3, 5) exhibits XANES spectra very different from those of Au(0) and Au(III) compounds
684 but strikingly similar to those of Au(I) S-bearing compounds such as Au₂S, Au-thiomalate or Au-
685 thiosulfate (not shown), as to the energy position, shape and amplitude of the white line at ~11,921
686 eV and the post-edge resonance at ~11,930 eV. These spectral features are characteristic of Au(I)
687 coordinated by two sulfur atoms in a linear geometry, typical for the majority of Au(I)-S
688 compounds (e.g., Pokrovski et al., 2009a). In addition, Py1 sample exhibits a very minor, yet
689 detectable, Au(0) feature at 11,945 eV (which can be quantified using LCF analyses below). The
690 third group of samples (Py3, 4; CoPy1) displays spectra with both Au(I) and Au(0) features. Note
691 also that the spectra of all pyrite samples are clearly distinct from those of Au(III)-bearing
692 compounds (e.g., KAuCl₄×2H₂O), which show a very intense feature at 11,920 eV due to the 2p-
693 5d transition, allowed in Au³⁺ but forbidden in Au⁺ (Berrodier et al., 2004; Pokrovski et al.,
694 2009b), together with other smaller post-edge resonances, which are all absent in the pyrite
695 spectra, demonstrating that no Au(III) occurs in our samples.

696 To further quantify the fractions of Au(0) and Au(I), linear combination fit (LCF)
697 analyses were performed on the pyrite spectra using as reference compounds metallic Au for
698 Au(0) and Au(I) sulfide (Au₂S), thiosulfate or thiomalate for Au(I) (Au₂S giving the best fit
699 quality). An example of LCF is given in Fig. A4. Owing to contrasting spectral features of Au(I)
700 and Au(0) in high-resolution mode, our method has a detection limit for Au(0) of ~3 mol% and an
701 uncertainty of ±3% on the value of Au(0) mole fraction, as evaluated using variable fit energy
702 ranges and different Au(I) compounds as standards. The fraction of chemically bound Au in pyrite
703 samples, Au(I), relative to total Au, Au(I)+Au(0), derived from LCF is reported in Table 3. These
704 data allow direct quantification of the absolute Au(I) concentrations, which are the product of
705 Au(I) mole fraction and the total invisible Au concentration from fluorescence spectra (as
706 determined using equation 2, section 2.6).

707

708 *3.4. Gold structural position in pyrite from FDMNES-simulated XANES spectra*

709

710 Comparisons of the experimental XANES spectra of Au-bearing pyrites with those of
711 reference compounds indicate that invisible chemically bound Au associated with pyrite is likely
712 present as S-Au(I)-S moieties (i.e., part of a molecule), probably associated with more distant
713 atoms (Fig. 4). However, the absence of stable Au-Fe-S-bearing solids with well-known
714 stoichiometry and structure whose spectra could be included in the comparison does not allow

715 unambiguous assessment of other possible Au coordination environments and their contribution to
716 the spectral signal. For example, some previous studies (e.g., Trigub et al., 2017) suggested that
717 chemically bound Au might also substitute for Fe or S in the pyrite structure; however, there is no
718 unambiguous proof for such models in the absence of adequate reference compounds.

719 To verify the impact of such potential substitutions on the XANES signal, we simulated
720 XANES spectra of Au in the Fe and S crystallographic sites of pyrite using the FDMNES code.
721 The Au-Fe/S distances and site geometries ranged from those of a regular pyrite structure, in
722 which Fe is octahedrally coordinated by 6 S atoms at 2.26 Å, and S is surrounded by 1 S and 3 Fe
723 atoms in a distorted tetrahedron, to those of relaxed structures, in which the Fe substitution site is
724 expanded to accommodate an AuS₆ octahedron with Au-S distances between 2.40 and 2.50 Å as
725 predicted by DFT simulations (Appendix A). The resulting calculated XANES spectra were found
726 to be only weakly sensitive to variations of Au-S and Au-Fe distances within the same
727 coordination geometry. The main factor affecting the XANES spectral shape, white line intensity,
728 and energy position is no doubt the Au nearest coordination sphere itself (i.e., number and cluster
729 geometry of the first-shell neighbors). It can be seen in Fig. 5a that calculated spectra for Au in Fe
730 and S sites in the pyrite structure are characterized by a very intense white line and significant
731 energy shifts as compared with the experimental spectra. The differences are far too large to be
732 attributed to imperfections of the FDMNES simulations or chosen structural models and
733 calculation parameters.

734 The FDMNES parameters have been validated by simulations of spectra of reference
735 compounds with known structures, which were found to adequately match the experimental
736 spectra (Fig. A5) and, in particular, the white-line intensity and position which is primarily
737 function of absorber first-shell coordination (Au site geometry and identity of neighboring atoms).
738 The effect of coordination environment is further demonstrated by simulations of XANES spectra
739 of isolated AuS_n clusters (2 < n < 6), with geometries ranging from linear AuS₂ to square-plane or
740 tetrahedral AuS₄ to octahedral AuS₆ with Au-S distances from 2.3 to 2.5 Å. It can be seen in Fig.
741 5b that there is a net increase in the white-line intensity with increasing Au coordination by S from
742 2 to 6, with the best match of the experimental pyrite spectra by a linear S-Au-S cluster (Au-S
743 distance 2.3 Å), which is the structural unit for Au(I) in most of its S-bearing solids and aqueous
744 complexes (Pokrovski et al., 2009a). The simple AuS₂ cluster has a narrower white line and a first
745 post-edge resonance maximum slightly shifted to lower energies compared to the experimental
746 pyrite spectrum, likely due to the presence of more distant atoms in the latter. The effect of such
747 atoms (H, S) on the XANES spectra of Au clusters may further be simulated by using the
748 optimized geometries of the Au(HS)₂⁻ and Au(HS)S₃⁻ complexes obtained using first principles

749 molecular dynamics in aqueous solution (Pokrovski et al., 2015). It can be seen in Fig. 5c that the
750 FDMNES simulated XANES spectra of these species do provide a better match of the
751 experimental spectrum than a simple AuS₂ cluster. Interestingly, there are small but distinctive
752 differences in the spectra of the two aqueous Au complexes (white-line energy shift and energy
753 and amplitude differences in the post-edge feature) suggesting that they might directly be
754 distinguished in aqueous solution in high-resolution mode. Finally, even a better match with the
755 experimental spectrum is obtained for an H-free S-Au-S₃ cluster that exhibits a white line
756 amplitude almost identical to the experimental spectrum and an energy shift of the maximum of
757 the first post-edge resonance toward that of the experiment (Fig. 5c). These similarities suggest
758 that Au(I) might be adsorbed on pyrite surface as such or similar complexes, and thus S₃²⁻ (and S₂²⁻
759) ions might favor gold scavenging by pyrite. More in-depth insight into the nature and structural
760 environment of gold species on the pyrite surface requires systematic molecular dynamics
761 simulations of the structures of adsorbed complexes, which is beyond the scope of the present
762 study.

763 Note that the effect of Au coordination on the XANES spectrum is neatly emphasized in
764 the high-resolution mode, which is necessary for unambiguously distinguishing the different Au
765 coordination environments in sulfur-bearing systems. In summary, both experimental and
766 FDMNES-simulated XANES spectra demonstrate that invisible Au in pyrite forms di-sulfide
767 clusters, likely bound to more distant S atoms, and no detectable incorporation of Au occurs in Fe
768 or S sites of the pyrite structure. The nature of this gold and its fluid-mineral partitioning are
769 discussed in the following sections.

770

771

4. Discussion

772

4.1. Interpretation of gold solubility and speciation in sulfur-bearing fluids

774

775 The interpretation of Au solubility measured in our experimental sulfate-sulfide systems in
776 terms of Au aqueous complexes is primarily based on knowledge of sulfur speciation itself, which
777 has been a subject of recent systematic research in similar systems at elevated temperatures and
778 pressures using in situ spectroscopic methods (Pokrovski and Dubrovinsky, 2011; Jacquemet et
779 al., 2014; Barré et al., 2017; Pokrovski and Dubessy, 2015; Pokrovski et al., 2015). These direct
780 spectroscopic data, combined with available thermodynamic properties of the major traditional S
781 species such as sulfate and sulfide, generally agree that the H₂S/HS⁻, S₃²⁻ and, potentially, S₂²⁻ ions

782 are the major ligands for gold. Figure 6 shows the distribution of S species calculated using the
783 available thermodynamic data, as a function of pH (equivalent to addition of HCl or KOH) at
784 450°C and 700 bar in a 0.5 m thiosulfate solution used in this study. The S_2^{2-} ion was also included
785 in these calculations based on the few available data points from in situ Raman spectroscopy
786 measurements of Pokrovski and Dubessy (2015) at 450°C in similar solutions (see Table A1 for
787 derivation of S_2^{2-} stability constant). It can be seen that the S species concentrations are strongly
788 pH dependent, resulting in a strong pH control on both Au complexes distribution and overall Au
789 solubility. In this discussion, we focus mostly on Au solubility data points obtained in this study at
790 450°C that represent a dataset large enough to allow a systematic examination of the effect of pH
791 and testing different Au speciation models. Our other experiments conducted at lower temperature
792 and lower S dissolved contents (Po1 and Po2, and CoPy1 and CoPy2 runs, Table 1 and 2) were
793 not considered in detail here because these few data points provide insufficient pH and ligand
794 concentration contrast in such dilute solutions to allow unambiguous discrimination among the
795 different Au speciation models.

796 Figure 7 compares the measured gold solubility at 450°C from this study with different
797 thermodynamic models. Model 1 includes both the $Au(HS)_2^-$ (dominant at neutral to basic pH) and
798 $Au(HS)S_3^-$ (dominant at acidic to neutral pH) complexes, whose thermodynamic properties have
799 been reported in recent studies based on Au solubility and in-situ XAS measurements in
800 hydrothermal S_3^{2-} -bearing solutions (Pokrovski et al., 2015). This model predicts Au solubility in
801 acidic conditions (pH<6, the neutral pH at 450°C, 700 bar being 6.05, see Fig. 6) within 50% of
802 the experimental value, but underestimates measured solubility at neutral-to-alkaline pH by a
803 factor of 5 to 10. For comparison, a traditional model involving $Au(HS)_2^-$ alone (model 2),
804 established on a large literature dataset obtained in H_2S/HS^- -dominated reducing solutions in
805 which S_3^{2-} is negligible (Pokrovski et al., 2014), largely underestimates, by a factor of 10 to 100,
806 the measured solubility over the whole pH range; this disagreement further confirms the
807 significance of Au- S_3^- complexes, particularly at pH<6, but points to the existence of some
808 additional Au species at more alkaline pH.

809 Because the S_2^{2-} ion attains its maximum concentration at pH 7-8, becoming comparable
810 with that of S_3^{2-} (Fig. 6), an S_2^{2-} -bearing complex, $Au(HS)S_2^-$ analogous to $Au(HS)S_3^-$, was
811 considered in an attempt to account for the measured elevated solubility in that pH range. The
812 stability constant of $Au(HS)S_2^-$ was adjusted to match the measured solubility at pH~8 at which
813 the disagreement of experiment with both model 1 and 2 is the largest. This new model involving
814 the three species, shown as model 3 in Fig. 7, largely overestimates the solubility at more acidic
815 pH, clearly demonstrating that $Au(HS)S_2^-$ cannot be a dominant Au species at pH >7. For

816 comparison, model 3bis shows the concentration of the same $\text{Au}(\text{HS})\text{S}_2^-$ complex calculated,
 817 following the analogy with $\text{Au}(\text{HS})\text{S}_3^-$ (Pokrovski et al., 2015) assuming an equilibrium constant
 818 of 1 for the ligand exchange reaction



820 This approximation is expected to be more reasonable than model 3 above since the chemical
 821 affinities for Au(I) of the HS^- , S_3^{2-} and S_2^{2-} ions of same electric charge and close formal redox
 822 state of S (-1, -0.33, and -0.5, respectively) should be similar (Pokrovski et al., 2015). Thus,
 823 $\text{Au}(\text{HS})\text{S}_2^-$ appears too weak to account for the elevated measured Au solubility at $\text{pH} > 6$. It
 824 cannot be excluded, however, that complexes with S_2^{2-} ion of different stoichiometry and charge
 825 than those considered here may contribute to Au solubility the neutral-to-alkaline region, but our
 826 dataset is too small to evaluate their impact and would require more systematic work.

827 Finally, model 4 considers $\text{Au}(\text{HS})_2^-$ alone, according to recent measurements of Trigub et
 828 al. (2017) in concentrated S-NaOH solutions using a similar batch-reactor quench technique as
 829 that of our study. These authors, however, used a simplistic S speciation model compared to that
 830 in our study, by ignoring S_3^{2-} and S_2^{2-} ions, as well as NaHS and Na(H)SO₄ ion pairs and
 831 Na₂SO₄(s) precipitation in their high-temperature alkaline solutions, which all may strongly affect
 832 predictions of both pH and redox potential and the resulting Au solubility interpretation.
 833 Combined with the artifact of the batch-reactor technique leading to overestimation of Au
 834 solubility as shown in this study (section 3.1; Fig. A1), their Au speciation model should be
 835 regarded with care. It can be seen in Fig. 7 that Trigub et al.'s model severely underestimates Au
 836 solubility at acidic pH, by at least a factor of 10, and overestimates Au solubility at neutral-to-
 837 alkaline pH by a factor of 2.

838 In summary, none of the models considered above can fully account for the measured Au
 839 solubility over the whole pH range at 450°C, and in particular in the alkaline region ($\text{pH} > 6$),
 840 which have not been covered before by direct systematic experiments. If the actual models
 841 qualitatively agree on the existence of Au complexes with HS^- , S_3^{2-} and, possibly, S_2^{2-} ligands, the
 842 exact stoichiometry and charge of these complexes, in particular those with S_2^{2-} , will require more
 843 systematic studies by both solubility and spectroscopic approaches.

844

845 *4.2. The speciation of invisible gold in pyrite and comparison with literature data*

846

847 *4.2.1. Invisible metallic gold*

848 Our findings of two major forms of invisible gold in pyrite, metallic gold submicron- to
 849 nanoparticles, Au(0), and chemically bound gold, Au(I), are in general agreement with the large

850 amount of literature published over almost 50 years (e.g., Boyle, 1969; Cabri et al., 1989; Reich et
851 al., 2005; Tauson et al., 2018; references therein). Both visible and invisible metallic gold
852 systematically found in our experimental pyrites is likely to have precipitated *i)* on cooling and/or
853 during the run due to minor thermal gradients favoring gold redistribution in the pyrite-fluid
854 system (Py runs), *ii)* upon FeS₂ formation by scavenging S from solution in experiments started
855 with FeS (Po runs), and *iii)* upon FeCl₂ injection inducing FeS₂ precipitation (CoPy runs), all these
856 phenomena leading to gold-supersaturated solutions favoring metal precipitation. The degree of
857 supersaturation, reaction time, and temperature may be the major factors controlling the size and
858 distribution of gold particles. As it has been recognized for a long time (Kouzmanov and
859 Pokrovski, 2012, for an overview and references therein), similar processes of fluid cooling, Fe-
860 rich rock sulfidation, and pyrite precipitation in nature lead to formation of metal gold. Another
861 possible process leading to nano-particle gold formation in pyrite and other sulfo-arsenides both in
862 nature and experiment may be fluid-assisted recrystallization and breakdown of chemically bound
863 Au that was initially incorporated into the mineral lattice or adsorbed on the surface. For example,
864 this process likely operated in orogenic gold deposits during pyrite and arsenopyrite metamorphic
865 recrystallization leading to expulsion of chemically bound metastable gold (e.g., Cook et al., 2009;
866 Large et al., 2009; Velasquez et al., 2014), and in mantle chromitites hosting platinum group
867 elements (PGE) that were subjected to fluid-assisted metamorphism leading to formation of
868 nanoparticles of Ru-Os-Ir alloys through thermal breakdown of PGE-bearing sulfide minerals
869 (e.g., González-Jiménez et al., 2015). In addition, slow crystal growth favoring migration and
870 clustering of adsorbed Au complexes on the surface of arsenopyrite might be a controlling factor
871 of nanoscale Au distribution, as recently evidenced by atom probe microscopy on arsenopyrite
872 from the Obiasi orogenic gold deposit (Fougerouse et al., 2016). Furthermore, because solid
873 solution miscibility is generally favored at elevated temperatures (e.g., Barton and Tolmin, 1966;
874 Barton, 1969), cooling itself may destabilize Au dissolved as a solid solution in the mineral lattice
875 leading to the formation of gold nanoparticles. Reheating such pyrites leads to dissolution of Au
876 nanoparticles as was shown by in situ experiments coupled with TEM observations on Au-bearing
877 pyrites from Carlin deposits (Reich et al., 2006). However, an opposite behavior was recently
878 reported by Trigub et al. (2017) who found formation of metallic gold while heating, in an
879 anhydrous FeS₂-S system, synthetic pyrite originally containing dominantly chemically bound
880 gold. Such behavior is at odds both with general knowledge of the thermal stability of most solid
881 solutions and the existing in-situ observations, thus indicating that chemically bound Au in their
882 pyrites is unlikely to be dissolved in the mineral lattice as an isomorphic substitution.

883

884 *4.2.2. Redox state of chemically bound gold*

885 If the mechanisms leading to occurrence of invisible *metallic gold* in pyrite are widely
886 recognized and explored in existing work as outlined above, the major debate remains on the exact
887 redox state, coordination, and structural position of *chemically bound gold*. Our data clearly
888 demonstrate that this type of invisible Au in pyrite occurs in nominally +1 redox state (Au(I)),
889 bound to sulfide and/or polysulfide ions, very similar to Au(I) in the fluid (such as Au(HS)S₃⁻) and
890 Au solids with reduced sulfur (Au₂S, Au-thiosulfate, Au-thiomalate). This finding is in agreement
891 with some previous work using Mössbauer spectroscopy (Marion et al., 1986; Friedl et al., 1995;
892 Palenik et al., 2004) and X-ray absorption spectroscopy on both natural (Simon et al., 1999) and
893 synthetic (Trigub et al., 2017) pyrites. Our results and previous data convincingly rule out the
894 significant presence of trivalent gold, Au(III), suggested in some studies on the basis of theoretical
895 considerations of cationic substitutions in the pyrite structure involving Fe²⁺, Au³⁺, As³⁺ and
896 vacancies (e.g., Arehart et al., 1993; Chouinard et al., 2005; Deditius et al., 2008). Note that the
897 nominally +3 redox state, Au(III), is known to only be stable in surficial oxygenated environments
898 (e.g., Berrodier et al., 2004) or chemical compounds with strongly electronegative ligands such as
899 F (Cotton and Wilkinson, 1988). Furthermore, trivalent gold association with reduced sulfur in
900 pyrite would be highly unlikely because no stable Au(III) sulfide compounds are known in
901 chemistry. Note, however, that the notion of redox state of a metal in covalent-bond dominated
902 compounds such as those in the Au-Fe-S(-As) system should be taken with care (e.g., Cabri et al.,
903 2000). Furthermore, in the presence of arsenic (arsenopyrite or lollingite), Au chemical state might
904 be different and a similar debate exists on those minerals (e.g., Cathelineau et al., 1989; Genkin et
905 al., 1998; Cabri et al., 2000), which is beyond the scope of our study that deals with As-poor
906 systems.

907

908 *4.2.3. Coordination and structural position of chemically bound gold*

909 Another major topic of debate is Au coordination and the corresponding position in the
910 pyrite structure. It should be emphasized that the only method enabling unambiguous
911 determination of Au site geometry and local atomic environment is XAS. Our HR-XANES
912 experimental spectra and FDMNES simulations collectively demonstrate that Au is coordinated in
913 its nearest shell by two S atoms, forming [-S-Au(I)-S-] moieties, similar to those known in most
914 Au sulfide and thiol-bearing compounds and Au-S species in hydrothermal solutions (e.g.,
915 Pokrovski et al., 2009a). Our findings agree with the pioneering XAS study of Simon et al. (1999)
916 on pyrites from Carlin-type gold deposits. Comparisons of their XANES data with reference
917 compounds would suggest a linear or square-planar coordination of Au with surrounding atoms,

918 but the insufficient resolution resulting in rather featureless spectra did not allow distinguishing
 919 among the possible neighboring atoms (Fe/S/As) in that early work. The Au L₃-edge XANES
 920 spectra of experimental pyrites of our study are also similar to those of natural pyrites from
 921 orogenic gold deposits, recently investigated using high-resolution synchrotron XRF and XANES
 922 spectroscopy, showing the presence of both Au(I) and Au(0) (Stromberg et al., 2019); however, no
 923 further development concerning Au(I) structural and coordination state was given in that study.
 924 Our interpretation disagrees with a recent XAS study of Trigub et al. (2017) who suggested, on the
 925 basis on XANES modeling and EXAFS fits of hydrothermally synthesized Au-bearing pyrites,
 926 that Au⁺ substitutes for Fe²⁺ in the pyrite structure. As in our study, however, their XANES
 927 spectra astonishingly resemble those of Au₂S, and the poor signal-to-noise ratio of their pyrite
 928 EXAFS spectra renders quantification of Au coordination number and Au-ligand interatomic
 929 distances uncertain (see Appendix A for detailed comparisons). Our data clearly rule out
 930 significant Au substitution in pyrite (at least As-free), which is also in agreement with studies of
 931 Tauson's group (Tauson, 2018, for overview) whose early experiments showed that only a few
 932 ppm of Au could be accommodated as a solid solution in the pyrite structure in Au metal-saturated
 933 systems. These authors further suggested, based on statistical analyses of bulk Au concentration
 934 and distribution as a function of grain size of synthetic and natural pyrites, that most Au is
 935 concentrated in so called 'non-autonomous' phase forming a layer of less than 1 μm thick at the
 936 pyrite surface. However, the exact composition of such a phase and Au structural and redox state
 937 remain unknown in the absence of direct spatially-resolved spectroscopic data. Further insight into
 938 the nature of chemically bound gold in pyrite may be gained from Au pyrite/fluid partition
 939 coefficients as discussed below.

940

941 *4.3. Gold partitioning between pyrite and hydrothermal fluid*

942

943 The direct data obtained in this study on Au concentrations ($C_{\text{Au(I)}}$) in the fluid phase and in
 944 coexisting pyrite allow derivation of the partition coefficient of chemically bound gold between
 945 pyrite and fluid defined as

$$946 D_{\text{py/fl}} = C_{\text{Au(I)}} \text{ (in pyrite)} / C_{\text{Au(I)}} \text{ (in fluid)} \quad (4).$$

947 A good linear correlation, apparent in Fig. 8 between Au(I) concentrations in the fluid phase and
 948 in pyrite from the exchange experiments at 450°C and 700 bar (Py and Po runs) in a wide range of
 949 aqueous Au contents (from 10s to 1,000s ppm), suggests an equilibrium exchange reaction. Such
 950 an exchange is little (if at all) dependent of the nature of Au(I) dominant species in the fluid
 951 (Au(HS)S₃⁻ vs Au(HS)₂⁻ vs Au-S₂⁻ complexes) and the initial solid phase (pyrite vs pyrrhotite).

952 The slope of the linear regression through zero of these data points corresponds to a partition
953 coefficient $D_{\text{py/fl}}$ of 0.15 ± 0.07 (1 SD). The co-precipitation experiment at the same P - T conditions
954 (CoPy3) yielded an uncertain $D_{\text{py/fl}}$ value ranging from <0 to ~ 4 , since Au(I) fraction in this
955 sample dominated by metallic Au was close to the detection limit (~ 3 mol% Au(I), Tables 3 and
956 4). Considering this uncertainty, these co-precipitation data overlap, within error, with the D
957 values from exchange experiments above. It seems thus likely that similar physical chemical
958 processes control Au(I) partitioning into pyrite in both types of experiment. The partition
959 coefficients of chemically bound Au for the lower-temperature co-precipitation experiments
960 (CoPy 1 and 2 at 350°C) are significantly higher, being of the order of 10 to 50 (Fig. 8, Table 4),
961 indicating that incorporation of Au(I) in pyrite is favored at lower temperatures. This experimental
962 finding is also in agreement with the higher abundance of chemically bound Au in pyrites from
963 low-to-moderate temperature hydrothermal deposits (e.g., Carlin-type, epithermal) compared to
964 pyrites from high-temperature magmatic or metamorphic deposits (porphyry, orogenic) that
965 contain dominantly metallic gold in ore (e.g., Deditius et al., 2014; references therein).

966 Our Au partitioning values from pyrite-fluid exchange experiments at 450°C are in
967 excellent agreement with those reported by Tauson et al. (2018) from experiments at the same T
968 and similar P ($D_{\text{py/fl}} = 0.3 \pm 0.2$). Interestingly, no effect of arsenic on Au incorporation in pyrite
969 was found in their study at similar conditions, in agreement with the paucity of Au-rich arsenian
970 pyrites in high-temperature hydrothermal settings. These authors interpreted such Au partitioning
971 as an isomorphic substitution in a non-autonomous submicron-thick solid phase at the pyrite
972 surface, but the structural and chemical position of Au in such a phase yet remain hypothetical.
973 The methods employed in our study do not have sufficient spatial resolution to verify the existence
974 of such a phase, which would require nano-scale in situ techniques, such as nano-beam XRD,
975 XRF, and XAS that will potentially be offered by the next generation of synchrotrons (e.g.,
976 Dimper et al., 2014). Furthermore, the robust linear correlation between dissolved and
977 incorporated Au(I) displayed in Fig. 8 suggests that the Au(I) activity (equivalent to
978 concentration) in pyrite increases with increasing the activity (or concentration) of aqueous Au(I)
979 in the fluid. Such a dependence rules out formation of Au proper solid phases (e.g., such as Au_2S)
980 on the pyrite surface, since Au activity in such a gold-dominated phase is constant, and thus must
981 be independent of Au activity in the fluid, which is not the case of our data shown in Fig. 8
982 displaying a clear positive correlation between Au in solution and pyrite. Even though our data do
983 not rule out Au substitution as an isomorphic impurity in a non-autonomous phase suggested in
984 Tauson's studies, a more plausible and simple explanation of the Au partitioning trends would be

985 formation of adsorbed S-Au-S complexes on the pyrite surface, similar to those in aqueous
986 solution as discussed below.

987

988 *4.4. Chemisorption control on Au(I) incorporation in As-poor pyrite*

989

990 Chemisorption has indeed been the most commonly invoked phenomenon to explain Au
991 scavenging by (arseno)pyrite (e.g., Fleet and Mumin, 1997), but detailed physical-chemical
992 mechanisms and driving forces of such sorption remain elusive. Only few experimental studies
993 devoted to Au sorption on sulfide mineral surfaces are available, none of them being conducted
994 above 90°C, to the best of our knowledge. Some studies (Mironov et al. 1982; Bancroft and
995 Hyland, 1990; Mycroft et al. 1995; Maddox et al. 1998; Mikhlin et al., 2011) employed acidic
996 Au³⁺ and Au⁺ chloride, cyanide, thiosulfate or citrate solutions, of little relevance to hydrothermal
997 sulfide-bearing fluids. They found that part of Au was rapidly reduced to the metallic state on the
998 surface of pyrite and arsenopyrite (depending of the relative stability of the Au aqueous
999 complexes). Some other studies (Scaini et al., 1998; Widler and Seward, 2002) examined sorption
1000 by iron sulfide minerals from Au(I) sulfide solutions, but reached rather different conclusions. For
1001 example, Scaini et al. (1998) found that Au sorption on FeS₂ increased with increasing pH
1002 accompanied by Au(I) reduction to metal, whereas Widler and Seward (2002) observed a
1003 moderate decrease of Au(HS)⁰ and Au(HS)₂⁻ adsorption on pyrite with increasing pH above 5,
1004 with no changes in redox state of adsorbed Au(I). Furthermore, these authors found that Au(I)
1005 adsorption on marcasite and pyrrhotite was significant only in acidic solutions (pH<4). Even
1006 though the temperature-composition parameters of our study are quite different from their work,
1007 there is a surprising similarity in acidity trends in our experiments, with the most acidic run (Py 1,
1008 pH~4.4) displaying a $D_{py/fl}$ value (~0.3) twice as high as the less acidic experiments (Table 4, Fig.
1009 8). Our values at acid pH are also close to those recently reported from fluid-pyrite Au exchange
1010 experiments in highly acidic S-H₂O solutions at 450°C ($D_{py/fl}$ ~1; Trigub et al., 2017) in line with a
1011 sorption control on Au incorporation in pyrite. Similar tendencies with pH were observed for
1012 Au(HS)⁰ and Au(HS)₂⁻ sorption on As₂S₃ and Sb₂S₃ at $T<90^{\circ}\text{C}$ (Renders and Seward, 1989).
1013 Because the isoelectric point of pyrite surface in H₂S-bearing aqueous solution is around pH~2 at
1014 ambient conditions (i.e., pyrite surface is positively charged at pH<2, and negatively charged at
1015 pH>2; Bebie et al., 1998; Widler and Seward, 2002), the strong adsorption of Au-sulfide
1016 negatively charged complexes dominant in S-bearing hydrothermal fluids investigated in this
1017 study (Au(HS)₂⁻, Au(HS)S₃⁻) should be different from simple electrostatically controlled outer-
1018 sphere sorption of cations or anions on oxide surfaces (i.e. loose electrostatic attraction of

1019 H₂O/H⁺/OH⁻ covered surface with the absorbing ions; e.g., Dzombak and Morel, 1990). Thus,
1020 Au(I) is expected to sorb via an inner-sphere mechanism, by forming direct Au-S-Fe or Au-S_n-Fe
1021 bonds with the pyrite surface, probably similar to that of arsenite, As(III) (As(OH)₃ and
1022 AsO(OH)₂⁻), sorption on FeS₂. Assuming the same surface site density for Au(I) as for As(III) (3.7
1023 sites/nm²; Bostick and Fendorf, 2002), it can be estimated that the maximal concentration of
1024 surface bound Au-S complexes for an ideal cubic-shape pyrite grain of 10 μm in size (having a
1025 surface area of 6×10×10 μm³), representative of our experiments, would reach as much as 20,000
1026 ppm Au if scaled to the mass of the grain. This sorption capacity is significantly superior to the
1027 Au(I) concentrations in pyrite measured in this study (<200 ppm Au(I) at 450°C, Table 3), thus
1028 supporting the linear trend with the concentration of Au(I) in the fluid shown in Fig. 8. Similar
1029 sorption capacities of pyrite *vis-à-vis* As(III) in aqueous solution were recently reported in
1030 siderite-to-pyrite replacement experiments at 200°C with As contents in pyrite reaching 10,000s
1031 ppm (Kusebauch et al., 2018), and independently by thermodynamic models of arsenian pyrite -
1032 fluid interactions at hydrothermal conditions (Xing et al., 2019). Furthermore, the plausibility of
1033 our adsorption mechanism is independently supported by natural observations of a general
1034 tendency to Au enrichment in small-grain pyrite from Carlin and MVT deposits (e.g., Reich et al.,
1035 2005; Tauson et al., 2018), since smaller grains offer larger surface areas favorable for adsorption.

1036 Gold hydrogen sulfide and radical ions may attach to pyrite surface by forming -S-S-
1037 bonds with sulfur atoms belonging to the corners of FeS₆ octahedrons (Fig. 9). Polysulfide sulfur
1038 is ubiquitous on pyrite surfaces as systematically demonstrated by direct XPS measurements in a
1039 wide range of solution compositions at near-ambient *T* (e.g., Nesbitt et al., 1998; Widler and
1040 Seward, 2002; references therein) and may be a key factor for scavenging Au(I) at higher *T* as
1041 well, further favored by existence of direct Au complexes with poly-sulfur ions (S₃⁻ and S₂⁻) in
1042 hydrothermal solution. The close resemblance of the XANES spectra of our Au-bearing pyrites to
1043 the simulated spectra of Au-S₃⁻ complexes (Fig. 5c) provides further support to this mechanism.
1044 The uptake of polysulfide Au species should also be favored during early stages of pyrite
1045 precipitation from hydrothermal fluids since pyrite formation occurs via polysulfide ion precursors
1046 (e.g., Schoonen and Barnes, 1991).

1047 Our laboratory experiments probe the key early stages of Au incorporation in pyrite ore
1048 such as Au scavenging by preexisting pyrite and simultaneous gold-pyrite precipitation that are
1049 fast phenomena compared to natural timescales of ore deposit formation and evolution. The fate of
1050 the sorbed Au-S species during the much slower processes of further pyrite crystal growth and
1051 ageing in natural systems remains an open question in pyrite geochemistry. It is expected that
1052 some part of these sorbed Au-S clusters are incorporated in defects and dislocations of the

1053 growing crystal owing to the lack of energetically favorable crystallographic position for Au(I) in
1054 the As-free pyrite structure. Other, likely major, part of sorbed Au would be reduced into Au(0)
1055 nanoparticles that may further migrate, grow, melt or get remobilized following cooling, thermal
1056 overprint, pressure changes, and fluid-assisted metamorphism (e.g., Reich et al., 2006; Velazquez
1057 et al., 2014; González-Jiménes et al., 2015). Future improvements in sensitivity and spatial
1058 resolution of in-situ spectroscopic techniques for ppm-level metal concentrations will enable more
1059 quantitative insight into the fate of invisible gold in pyrite during such processes.

1060 In the presence of significant amounts of arsenic in pyrite, however, the mechanisms and
1061 driving forces of Au scavenging and long-term storage may be different, since arsenic may
1062 considerably affect both surface electrical and chemical properties (e.g., Mironov et al., 1981;
1063 Moeller and Kersten, 1994) and the crystal structure, for example, facilitating Au incorporation as
1064 a solid solution. Although As-bearing systems are beyond the scope of this study, our new data on
1065 fluid-pyrite partition coefficients of Au in As-poor systems indirectly support the key role of
1066 arsenic in gold enrichment in iron sulfide minerals in nature, as will be shown below.

1067

1068 *4.5. Role of arsenic in gold incorporation in pyrite*

1069

1070 The partition coefficients of Au(I) obtained in this study allow prediction of Au dissolved
1071 contents in As-poor pyrite in nature. Detailed Au-As systematics of pyrites from various gold
1072 deposits (Carlin, orogenic, porphyry, epithermal, OICG, VHMS, and Witwatersrand) has recently
1073 been provided by Deditius et al. (2014). Their analysis demonstrates that invisible Au and As are
1074 generally positively correlated in pyrite at As contents above 0.01-0.1 wt% and that the solubility
1075 limit of chemically bound Au in arsenian pyrite is defined by an Au/As atomic ratio of 0.02
1076 independently of the geochemical environment. Both Au and As tenors in natural pyrite generally
1077 increase with decreasing T in the range 500-200°C.

1078 These natural observations are in excellent agreement with our experimental data showing
1079 Au(I) pyrite-fluid partition coefficients at 350°C ($D_{py/fl} \sim 10-50$) significantly greater than at 450°C
1080 ($D_{py/fl} \sim 0.2$). Gold concentrations in hydrothermal fluids forming porphyry-epithermal and
1081 orogenic deposits, as inferred from both direct fluid inclusion analyses and thermodynamic
1082 calculations of gold solubility, are typically less than 1 ppm, even though some high-temperature
1083 sulfur-rich magmatic fluids ($\geq 450^\circ\text{C}$) may exceptionally contain up to 30 ppm Au (e.g.,
1084 Kouzmanov and Pokrovski, 2012; Garofalo et al., 2014; Pokrovski et al., 2014). Combining these
1085 natural concentrations with the $D_{py/fl}$ values derived in this study at 450°C yields Au(I) tenors in
1086 pyrite of less than 3 ppm Au in high-temperature porphyry and orogenic environments. This is in

1087 agreement with the low Au(I) tenors in As-poor pyrites from such settings, which are largely
1088 dominated by metallic gold in pyrite ore. For lower temperature epithermal, Carlin, volcanic
1089 massive sulfide (VMS), and some orogenic deposits ($\leq 350^\circ\text{C}$) that often lack analyzable fluid
1090 inclusions, there is virtually no direct data on Au fluid contents; nevertheless, Au fluid-phase
1091 concentrations are expected to be even smaller (< 0.1 ppm Au) due to the much lower sulfide
1092 mineral solubility (pyrite and pyrrhotite) and the resulting low concentrations of reduced sulfur
1093 aqueous species ($\text{H}_2\text{S}/\text{HS}^-$, S_3^{2-}), which are the key ligands for Au transport as shown in this study
1094 and previous work (e.g., Kouzmanov and Pokrovski, 2012; Pokrovski et al., 2015; references
1095 therein). Such sub-ppm Au(I) fluid concentrations, combined with our $D_{\text{py/fl}}$ values obtained at
1096 350°C (~ 10 - 50), would correspond to pyrite Au(I) contents of less than a few ppm. These
1097 predicted Au concentrations are in excellent agreement with the solubility limit of chemically
1098 bound gold in *arsenic-free pyrite* of 2 ppm Au (Reich et al., 2005). By contrast, our predicted
1099 values are 1 to 3 orders of magnitude lower, on average, than the Au concentrations analyzed in
1100 natural *arsenian pyrites* (> 0.01 - 0.1 wt% As) from these environments (Deditius et al., 2014;
1101 references therein).

1102 Therefore, our experimental data obtained in As-free systems indirectly support the key
1103 role of arsenic in gold enrichment in arsenian pyrites and arsenopyrites from such deposits. Our
1104 results provide a sound physical-chemical interpretation of the famous wedge-shaped pattern of
1105 Au solubility in arsenian pyrite, established in the seminal work of Reich et al. (2005) on the basis
1106 of pyrite analyses from Carlin-type deposits, and more recently shown to be applicable to other
1107 types of Au deposits. According to Reich et al.'s gold solubility model in pyrite, at low As
1108 contents relevant to our study, Au(I) solubility is low (< 2 ppm) and independent of As pyrite
1109 content up to ~ 0.01 wt% As, but increases proportionally to As at higher As contents (Fig. 9). Our
1110 direct partitioning and spectroscopic data are in quantitative agreement with the lower-As part of
1111 the solubility curve where Au(I) incorporation in pyrite is controlled by chemisorption as Au-
1112 (poly)sulfide complexes, partly incorporated in defects and dislocations by the growing pyrite
1113 crystal, and partly rejected from the structure by reduction to Au(0) during further pyrite life. In
1114 contrast, for As-richer pyrites our data imply a fundamental change in the mechanism of Au
1115 scavenging by the mineral. Arsenic would presumably favor both chemisorption and incorporation
1116 of gold into the crystal structure as isomorphic constituent, but the physical-chemical mechanisms
1117 and driving forces of this 'arsenic effect' and Au exact structural position yet remain to be fully
1118 understood and quantified via integrated experimental, spectroscopic, and modeling studies.

1119

1120

5. Concluding remarks

1121

1122

1123 The key points of this study are the following:

1124 A combination of experimental, analytical and modeling approaches used in this work
1125 enables new insight into one of the oldest enigmas of Ore Deposit Research, the nature of invisible
1126 gold in pyrite. We show that gold is incorporated from hydrothermal fluids into As-poor pyrite
1127 both as native metal, Au(0) in the form of nano- and submicron particles, and as chemically bound
1128 gold of a nominal redox state of +1, Au(I).

1129 High-resolution XANES experimental and simulated spectra of Au-bearing pyrites
1130 demonstrate that Au(I) is coordinated with two nearest sulfur atoms in a linear geometry, similar
1131 to Au(I) complexes with the HS⁻ and S₃²⁻ ligands dominant in hydrothermal ore-forming fluids.
1132 The Au(I) incorporation in pyrite at molecular level is likely to proceed via specific sorption of S-
1133 Au-S aqueous species on the pyrite surface with formation of polysulfide moieties, [-S-Au-S-(S-
1134)_n]. Our results rule out, at least in As-poor systems, the commonly accepted paradigm postulating
1135 Au⁺ substitution for Fe²⁺ in the pyrite structure with formation of a solid solution as the mode of
1136 chemically bound Au incorporation in pyrite.

1137 Combining the derived Au(I) content in pyrite with accurate Au concentration
1138 measurements in the coexisting hydrothermal fluid from our experiments allows generation of a
1139 first set of Au(I) partition coefficients between fluid and pyrite at *P-T* conditions typical of many
1140 types of gold deposits. These coefficients imply relatively low dissolved gold contents, of less
1141 than a few ppm Au, in As-poor pyrites (<0.01 wt% As), in full agreement with numerous natural
1142 observations. Our estimations contrast with the elevated invisible Au contents, of 100 to 1,000s
1143 ppm Au, commonly recorded in As-rich pyrites (>1 wt% As) and arsenopyrites (10s wt% As) in
1144 many ore deposits; they thus highlight the fundamental control of As on Au incorporation in these
1145 minerals. Quantitative assessment of the true role of arsenic in the gold fate in fluid-mineral
1146 systems could only be achieved using a combination of cutting-edge experimental, spectroscopic
1147 and modeling approaches.

1148 Furthermore, the results of this study highlight limitations of the existing thermodynamic
1149 and speciation models of Au in S-bearing hydrothermal fluids that still persist despite more than
1150 50 years of extensive research. In addition to 'traditional' Au complexes with HS⁻ ligands, our
1151 data confirm the existence, in high-temperature fluids (≥450°C), of Au species with other ligands
1152 such as S₃²⁻ and S₂²⁻ ions whose nature, stability, and role in Au transport and scavenging by
1153 sulfide minerals will require future integrated research.

1154
1155
1156

Acknowledgments

1157 This work was funded by the French National Research Agency (grants Radicals – ANR-16-CE31-0017 and
1158 SOUMET – ANR-2011-Blanc SIMI 5-6 009), the Institut des Sciences de l'Univers of the Centre National de la
1159 Recherche Scientifique (grants OrPy-CESSUR and AsOrPy-CESSUR), and the Institut Carnot ISIFoR (grant OrPet).
1160 We acknowledge the European Synchrotron Radiation Facility (ESRF) for providing access to beamtime and
1161 infrastructure. DFT calculations were performed using HPC resources from CALMIP (grant 2018-P1037). We thank
1162 P. Gisquet, A. Castillo, S. Mounic, P. Besson, C. Causserand, A. Marquet, C. Duquenoy, F. Candaudap, J. Chmelef,
1163 M. Henry, L. Menjot, J.-F. Ména, F. de Parseval, C. Laskar, A. Colin, I. Kieffer, E. Lahera, W. Del Net for their
1164 professional help with the tough hydrothermal experiments, exhausting synchrotron measurements, and tedious
1165 sample preparations and chemical analyses. We are grateful to A.-M. Cousin for the help with figure preparation.
1166 Special thanks go to Y. Joly for advice on XANES spectra modeling and to Y. Shvarov for guidance with
1167 thermodynamic calculations. We thank Editors H. Chen and C. Ciobanu for handling this manuscript and reviewers M
1168 Reich, P. Garofalo, and an anonymous referee for their insightful comments that greatly improved this article.
1169

References

- 1170
1171
1172 Adams, M.D., ed., 2005. *Advances in gold ore processing*. Elsevier.
- 1173 Akinfiyev, N.N., Diamond, L.W., 2003. Thermodynamic description of aqueous nonelectrolytes at infinite dilution
1174 over a wide range of state parameters. *Geochim. Cosmochim. Acta* 67, 613-627.
- 1175 Amestoy, P. R., Guermouche, A., L'Excellent, J.-Y., Pralet, S., 2006. Hybrid scheduling for the parallel solution of
1176 linear systems. *Parallel Computing* 32 (2), 136-156.
- 1177 Arehart, G.B., Chryssoulis, S.L., Kesler, S.E., 1993. Gold and arsenic in iron sulfides from sediment-hosted
1178 disseminated gold deposits: Implication for depositional processes. *Econ. Geol.* 88, 171-185.
- 1179 Bancroft, G.M., Hyland, M.M., 1990. Spectroscopic studies of adsorption/reduction reactions of aqueous metal
1180 complexes on sulphide surfaces. *Rev. Miner. Geochem.* 23, 511-558.
- 1181 Barré, G., Truche, L., Bazarkina, E.F., Michels, R., Dubessy, J., 2017. First evidence of the trisulfur radical ion S_3^-
1182 and other sulfur polymers in natural fluid inclusions. *Chem. Geol.* 462, 1-14.
- 1183 Barton, P.B. Jr., 1969. Thermochemical study of the system Fe-As-S. *Geochim. Cosmochim. Acta* 33, 841-857.
- 1184 Barton, P.B. Jr., Toulmin III, P., 1966. Phase relations involving sphalerite in the Fe-Zn-S system. *Econ. Geol.* 61,
1185 815-849.
- 1186 Bebie, J., Schoonen, M.A.A., Fuhrmann, M., Strongin, D.R., 1998. Surface charge development on transition metal
1187 sulfides: An electrokinetic study. *Geochim. Cosmochim. Acta* 62, 633-642.
- 1188 Berrodier, I., Farges, F., Benedetti, M., Winterer, M., Brown, Jr., G.E., Deveugèle, M., 2004. Adsorption
1189 mechanisms of trivalent gold on iron- and aluminum-(oxy)hydroxides. Part 1: X-ray absorption and raman
1190 scattering spectroscopic studies of Au(III) adsorbed on ferrihydrite, goethite, and boehmite. *Geochim.*
1191 *Cosmochim. Acta* 68, 3019-3042.
- 1192 Boiron, M.C., Cathelineau, M., Trescases, J.J., 1989. Conditions of gold-bearing arsenopyrite crystallization in the
1193 Villeranges basin, Marche-Combrailles shear zone, France. A mineralogical and fluid inclusion study. *Econ.*
1194 *Geol.*, 84, 1340–1362.
- 1195 Bostick, B., Fendorf, S., 2003. Arsenite sorption on troilite (FeS) and pyrite (FeS₂). *Geochim. Cosmochim. Acta* 67,
1196 909-921.
- 1197 Boyle, R.W., 1969. Hydrothermal transport and deposition of gold. *Econ. Geol.* 64, 112-115.
- 1198 Bunau, O., Joly, Y., 2009. Self-consistent aspects of x-ray absorption calculations. *J. Phys.: Condens. Matter* 21,
1199 345501.
- 1200 Cabri, L.J., Newville, M., Gordon, R.A., Crozier, E.D., Sutton, S.R., McMahon, G., Jiang, D.-T., 2000. Chemical
1201 speciation of gold in arsenopyrite. *Can. Mineral.* 38, 1265–1281.
- 1202 Cabri, L.J., Chryssoulis, S.L., De Villiers, J.P.R., Laflamme J.H.G., Buseck, P.R., 1989. The nature of “invisible”
1203 gold in arsenopyrite. *Can. Mineral.* 27, 353-362.
- 1204 Cathelineau, M., Boiron, M-C., Holliger, P., Marion, P., Denis, M., 1989. Gold in arsenopyrites: Crystal chemistry,
1205 location and state, physical and chemical conditions of deposition. *Econ. Geol. Monograph* 6, 328-341.
- 1206 Cepedal, A., Fuertes-Fuente, M., Martin-Izard, A., Gonzalez-Nistal, S., Barrero, M., 2008. Gold-bearing As-rich
1207 pyrite and arsenopyrite from the El Valle gold deposit, Asturias, northwestern Spain. *Can. Miner.* 46, 233-247.
- 1208 Chase, M.W., Jr., 1998. NIST-JANAF Thermochemical Tables, Fourth Edition. *J. Phys. Chem. Ref. Data, Monograph*
1209 No. 9; available at <http://webbook.nist.gov/chemistry>.
- 1210 Chouinard, A., Paquette, J., Williams-Jones, A.E., 2005. Crystallographic controls on trace-element incorporation in
1211 auriferous pyrite from the Pascua epithermal high-sulfidation deposit, Chile-Argentina. *Can. Min.* 43, 951-963.
- 1212 Cook, N.J., Chryssoulis, S.L., 1990. Concentrations of «invisible» gold in the common sulfides. *Can. Mineral.* 28, 1–
1213 16.
- 1214 Cook, N.J., Ciobanu, C.L., Mao, J., 2009. Textural control on gold distribution in As-free pyrite from the Dongping,
1215 Huangtuliang and Hougou gold deposits, North China craton (Hebei Province, China). *Chem. Geol.* 264, 101-
1216 121.
- 1217 Cotton, A.F., Wilkinson, G., 1988. *Advanced Inorganic Chemistry*. Fifth Edition, Wiley.
- 1218 Deditius, A.P., Utsunomiya, S., Renock, D., Ewing, R.C., Ramana, C.V., Becker, U., Kesler, S.E., 2008. A proposed
1219 new type of arsenian pyrite: Composition, nanostructure and geological significance. *Geochim. Cosmochim.*
1220 *Acta* 72, 2919-2933.
- 1221 Deditius, A.P., Utsunomiya, S., Reich, M., Kesler, S.E., Ewing, R.C., Hough, R., Walshe, J., 2011. Trace metal
1222 nanoparticles in pyrite. *Ore Geol. Rev.* 42, 32-46.

- 1223 Deditius, A.P., Reich, M., Kesler, S.E., Utsunomiya, S., Walshe, J., Chryssoulis, S.L., Ewing, R.C., 2014. The
 1224 coupled geochemistry of Au and As in pyrite from hydrothermal deposits. *Geochim. Cosmochim. Acta* 140,
 1225 644-670.
- 1226 Den Besten, J., Jamieson, D. N., Ryan, C. G., 1999. Lattice location of gold in natural pyrite crystals. *Nucl. Instrum.*
 1227 *Meth. B* 152, 135-144.
- 1228 Dimper, R., Reichert, H., Raimondi, P., Ortiz, L.S., Sette, F., Susini, J., 2014. ESRF upgrade program phase II (2015-
 1229 2022). The Orange Book, ESRF. http://www.esrf.eu/Apache_files/Upgrade/ESRF-orange-book.pdf.
- 1230 Driesner, T., Heinrich, C.A., 2007. The system H₂O–NaCl. Part I: Correlation formulae for phase relations in
 1231 temperature–pressure–composition space from 0 to 1000 °C, 0 to 5000 bar, and 0 to 1 XNaCl: *Geochim.*
 1232 *Cosmochim. Acta* 71, 4880-4901.
- 1233 Dzombak, D.A., Morel, F.M.M., 1990. *Surface Complexation Modeling: Hydrous Ferric Oxide*. Wiley.
- 1234 Fleet, M.E., Mumin, A.H., 1997. Gold-bearing arsenian pyrite and marcasite and arsenopyrite from Carlin Trend gold
 1235 deposits and laboratory synthesis. *Am. Mineral.* 82, 182–193.
- 1236 Fougereuse, D., Reddy, S.M., Saxey, D.W., Rickard, W.D.A., van Riessen, A., Micklethwaite, S., 2016. Nanoscale
 1237 gold clusters in arsenopyrite controlled by growth rate not concentration: Evidence from atom probe
 1238 microscopy. *Amer. Miner.* 101, 1916-1919.
- 1239 Friedl, J., Wagner, F.E., Wang, N., 1995. On the chemical state of combined gold in sulfidic ores: conclusions from
 1240 Mössbauer source experiments. *Neues Jahrb. Mineral. Abh.* 169, 279-290.
- 1241 Garofalo, P.S., Fricker, M.B., Günther, D., Barsani, D., Lottici, P.P., 2014. Physical-chemical properties and metal
 1242 budget of Au-transporting hydrothermal fluids in orogenic deposits. *Geol. Soc. London Spec. Publ.* 402, 71-
 1243 102.
- 1244 Genkin, A.D., Bortnikov, N.S., Cabri, L.J., Wagner, F.E., Stanley, C.J., Safonov, Y.G., McMahon, G., Friedl, J.,
 1245 Kerzin, A.L., Gamyarin, G.N., 1998. A multidisciplinary study of invisible gold in arsenopyrite from four
 1246 mesothermal gold deposits in Siberia, Russian Federation. *Econ. Geol.* 93, 463–487.
- 1247 Goldschmidt, V.M., 1937. The principles of distribution of chemical elements in minerals and rocks. The seventh
 1248 Hugo Müller lecture, delivered before the Chemical Society on March 17th, 655–673.
- 1249 Guda, S.A., Guda, A.A., Soldatov M.A., Lomachenko K.A., Bugaev, A.L., Lamberti, C., Gawelda, W., Bressler, C.,
 1250 Smolentsev, G., Soldatov, A.V., Joly, Y., 2015. Optimized finite difference method for the full-potential
 1251 XANES simulations. Application to molecular adsorption geometries in MOFs and metal-ligand intersystem
 1252 crossing transients. *J. Chem. Theory Comput.* 11, 4512-4521.
- 1253 Guillong, M., Meier, D. L., Allan, M. M., Heinrich, C. A., and Yardley, B. W. D., 2008. SILLS: A MATLAB-based
 1254 program for the reduction of laser ablation ICP-MS data of homogeneous materials and inclusions. In: *Laser*
 1255 *Ablation ICP-MS in the Earth Sciences: Current Practices and Outstanding Issues* (Sylvester P., ed.). *Miner.*
 1256 *Ass. Can. Short Course Ser.* 40, 328–333.
- 1257 Gundlach-Graham, A., Garofalo, P. S., Schwarz, G., Redi, D., and Günther, D., 2018. High-resolution, quantitative
 1258 element imaging of an upper crust, low-angle cataclase (Zuccale fault, Northern Apennines) by laser ablation
 1259 ICP time-of-flight mass spectrometry. *Geostand. Geoanal. Res.* 42, 559-574.
- 1260 Heinrich, C.A., Eadington, P.J., 1986. Thermodynamic predictions of the hydrothermal chemistry of arsenic and their
 1261 significance for the paragenetic sequence of some cassiterite-arsenopyrite-base metal sulfide deposits. *Econ.*
 1262 *Geol.* 81, 511-529.
- 1263 Helgeson, H.C., Kirkham, D.H., Flowers, G.C., 1981. Theoretical prediction of the thermodynamic behavior of
 1264 aqueous electrolytes at high pressures and temperatures: IV. Calculation of activity coefficients, osmotic
 1265 coefficients and apparent molal and relative partial molal properties to 600° C and 5 kb. *Amer J Sci* 281, 1249-
 1266 1516.
- 1267 Jacquemet, N., Guillaume, D., Zwick, A., Pokrovski, G.S., 2014. In situ Raman spectroscopy identification of the S₃⁻
 1268 ion in S-rich hydrothermal fluids from synthetic fluid inclusions. *Amer. Miner.* 99, 1109-1118.
- 1269 Johnson, J.W., Oelkers, E.H., Helgeson, H.C., 1992. SUPCRT92: A software package for calculating the standard
 1270 molal thermodynamic properties of minerals, gases, aqueous species, and reactions from 1 to 5000 bar and 0 to
 1271 1000°C. *Computers & Geosci.* 18, 899-947. Updated version based on a series of subsequent papers reporting
 1272 HKF parameters for most ions and aqueous complexes is available on line at <http://geopig.asu.edu/index.html#>.
- 1273 Joly, Y., 2001. X-ray absorption near-edge structure calculations beyond the muffin tin approximation. *Phys. Rev.*
 1274 *B* 63, 125120.
- 1275 Joly, Y., 2018. FDMNES User’s Guide. <http://neel.cnrs.fr/spip.php?rubrique1007&lang=en>.
- 1276 Kokh, M.A., Lopez, M., Gisquet, P., Lanzanova, A., Candaudap, F., Besson, P., Pokrovski, G.S., 2016. Combined
 1277 effect of carbon dioxide and sulfur on vapor-liquid partitioning of metals in hydrothermal systems. *Geochim.*
 1278 *Cosmochim. Acta* 187, 311-333.

- 1279 Kokh, M.A., Akinfiev, N.N., Pokrovski, G.S., Salvi, S., Guillaume, D., 2017. The role of carbon dioxide in the
1280 transport and fractionation of metals by geological fluids. *Geochim. Cosmochim. Acta* 197, 433-466.
- 1281 Kouzmanov, K., Pokrovski, G.S., 2012. Hydrothermal controls on metal distribution in Cu(-Au-Mo) porphyry
1282 systems. *Society of Economic Geologists Special Publication* 16 (22), 573-618.
- 1283 Kusebauch, C., Oelze, M., Gleeson, S.A., 2018. Partitioning of arsenic between hydrothermal fluid and pyrite during
1284 experimental siderite replacement. *Chem. Geol.* 500, 136-147.
- 1285 Large, R.R., Danyushevsky, L., Hollit, C., Maslennikov, V., Meffre, S., Gilbert, S., Bull, S., Scott, R., Emsbo, P.,
1286 Thomas, H., Singh, B., Foster, J., 2009. Gold and trace element zonation in pyrite using a laser imaging
1287 technique: Implications for the timing of gold in orogenic and Carlin-style sediment-hosted deposits. *Econ.*
1288 *Geol.* 104, 635-668.
- 1289 Le Pape, P., Blanchard, M., Juhin, A., Rueff, J-P., Manoj, D., Morin, G., Cabaret, D., 2018. Local environment of
1290 arsenic in sulfide minerals: insights from high-resolution X-ray spectroscopies, and first-principles calculations
1291 at the As K-edge. *J. Anal. At. Spectrom.* 33, 2070-2082.
- 1292 Llorens, I., Lahera, E., Del Net, W., Proux, O., Braillard, A., Hazemann, J.-L., Prat, A., Testemale, D., Dermigny, Q.,
1293 Gelebart, F., Morand, M., Shukla, A., Bardou, N., Ulrich, O., Arnaud, S., Berar, J.-F., Boudet, N., Caillot, B.,
1294 Chaurand, P., Rose, J., Doelsch, E., Martin, P., Solari, P.L., 2012. High energy resolution five-crystal
1295 spectrometer for high quality fluorescence and absorption measurements on an x-ray absorption spectroscopy
1296 beamline. *Rev. Sci. Instruments* 83, 063104.
- 1297 Maddox, L.M., Bancroft, G.M., Scaini, M.J., Lorimer, J.W., 1998. Invisible gold: Comparison of Au deposition on
1298 pyrite and arsenopyrite. *Amer. Mineral.* 83, 1240-1245.
- 1299 Manceau, A., Merkulova, M., Murdzek, M., Batanova, V., Baran, R., Glatzel, P., Saikia, B.K., Paktunc, D., Lefticariu,
1300 L., 2018. Chemical forms of mercury in pyrite: Implications for predicting mercury releases in acid mine
1301 drainage settings. *Environ. Sci. Technol.* 52(18), 10286-10296.
- 1302 Mao, S.H., 1991. Occurrence and distribution of invisible gold in a Carlin-type gold deposit in China. *Amer. Mineral.*
1303 76, 1964-1972.
- 1304 Marion, P.H., Regnard, J-R., Wagner, F.E., 1986. Etude de l'état chimique de l'or dans les sulfures aurifères par
1305 spectroscopie Mössbauer de ¹⁹⁷Au. *Comptes Rendus Acad. Sci. (Paris)* 302 II, 571-574.
- 1306 Marsden, J.O., House, C.I., 2009. *The Chemistry of Gold Extraction*. 2nd edition, Society for Mining, Metallurgy, and
1307 Exploration, Inc.
- 1308 Mikhlin, Y., Romanchenko, A., Likhatski, M., Karacharov, A., Erenburg, S., Trubina, S., 2011. Understanding the
1309 initial stages of precious metals precipitation: Nanoscale metallic and sulfidic species of gold and silver on
1310 pyrite surfaces. *Ore Geol. Rev.* 42, 47-54.
- 1311 Mironov, A.G., Zhmodik, S.M., Maksimova, E.A., 1981. An experimental investigation of the sorption of gold by
1312 pyrites with different thermoelectric properties. *Geochim. International*, 18, 153-160.
- 1313 Möller, P., Kersten, G., 1994. Electrochemical accumulation of visible gold on pyrite and arsenopyrite surfaces.
1314 *Mineral. Deposita* 29, 404-413.
- 1315 Nesbitt, H.W., Bancroft, G.M., Pratt, A.R., Scaini, M.J., 1998. Sulfur and iron surface states on fractured pyrite
1316 surfaces. *Amer. Miner.* 83, 1067-1076.
- 1317 Oelkers, E.H., Benezeth, P., Pokrovski, G.S., 2009. Thermodynamic databases for water-rock interaction. *Rev. Miner.*
1318 *Geochem.* 70, 1-46.
- 1319 Palenik, C.S., Utsunomiya, S., Reich, M., Kesler, S.E., Wang, L., Ewing, R.C., 2004. "Invisible" gold revealed: direct
1320 imaging of gold nanoparticles in a Carlin-type deposit. *Am. Mineral.* 89, 1359-1366.
- 1321 Pokrovski, G.S., Borisova, A.Y., Harrichoury, J.-C., 2008. The effect of sulfur on vapor-liquid fractionation of metals
1322 in hydrothermal systems. *Earth Planet. Sci. Lett.* 266, 345-362.
- 1323 Pokrovski, G.S., Dubrovinsky, L.S., 2011. The S₃⁻ ion is stable in geological fluids at elevated temperatures and
1324 pressures. *Science* 331, 1052-1054
- 1325 Pokrovski, G.S., Kara, S., Roux, J., 2002. Stability and solubility of arsenopyrite, FeAsS, in crustal fluids. *Geochim.*
1326 *Cosmochim. Acta* 66, 2361-2378.
- 1327 Pokrovski, G.S., Tagirov, B.R., Schott, J., Hazemann, J-L., Proux, O., 2009a. A new view on gold speciation in
1328 sulfur-bearing hydrothermal fluids from in-situ X-ray absorption spectroscopy and quantum-chemical
1329 modeling. *Geochim Cosmochim Acta* 73, 5406-5427.
- 1330 Pokrovski, G.S., Tagirov, B.R., Schott, J., Bazarkina, E.F., Hazemann, J.-L., Proux, O., 2009b. An in situ X-ray
1331 absorption spectroscopy study of gold-chloride complexing in hydrothermal fluids. *Chem. Geol.* 259, 17-29.
- 1332 Pokrovski, G.S., Akinfiev, N.N., Borisova, A.Y., Zotov, A.V., Kouzmanov, K., 2014. Gold speciation and transport in
1333 geological fluids: insights from experiments and physical-chemical modelling. *Geol. Soc. Spec. Publ. London.*
1334 402, 9-70.

- 1335 Pokrovski, G.S., Dubessy, J., 2015. Stability and abundance of the trisulfur radical ion S_3^- in hydrothermal fluids.
 1336 Earth Planet. Sci. Lett. 411, 298-309.
- 1337 Pokrovski, G.S., Kokh, M.A., Guillaume, D., Borisova, A.Y., Gisquet, P., Hazemann, J.-L., Lahera, E., Del Net, W.,
 1338 Proux, O., Testemale, D., Haigis, V., Jonchière, R., Seitsonen, A.P., Ferlat, G., Vuilleumier, R., Saitta, A.M.,
 1339 Boiron, M.-C., Dubessy, J., 2015. Sulfur radical species form gold deposits on Earth. Proc. Nat. Acad. Sci
 1340 USA 112, 13484-13489.
- 1341 Proux, O., Biquard, X., Lahera, E., Menthonnex, J.-J., Prat, A., Ulrich, O., Soldo, Y., Trévisson, P., Kapoujvan, G.,
 1342 Perroux, G., Taunier, P., Grand, D., Jeantet, P., Deleglise, M., Roux, J.-P., Hazemann, J.-L., 2005. FAME: a
 1343 new beamline for X-ray absorption investigations of very diluted systems of environmental, material and
 1344 biological interests. Phys. Scripta T115, 970-973.
- 1345 Proux, O., Lahera, E., Del Net, W., Kieffer, I., Rovezzi, M., Testemale, D., Irar, M., Thomas, S., Aguilar-Tapia, A.,
 1346 Bazarkina, E. F., Prat, A., Tella, M., Auffan, M., Rose, J., Hazemann, J.-L., 2017. High Energy Resolution
 1347 Fluorescence Detected X-ray Absorption Spectroscopy: a new powerful structural tool in environmental
 1348 biogeochemistry sciences. J. Environ. Quality 46, 1146-1157.
- 1349 Ravel, B., Newville, M., 2005. ATHENA, ARTEMIS, HEPHAESTUS: data analysis for X-ray absorption
 1350 spectroscopy using IFEFFIT. J. Synchrotron Rad. 12, 537-541.
- 1351 Reich, M., Kesler, S.E., Utsunomiya, S., Palenik, C.S., Chryssoulis, S.L., Ewing, R.C., 2005. Solubility of gold in
 1352 arsenian pyrite. Geochim. Cosmochim. Acta 69, 2781-2796.
- 1353 Reich, M., Chryssoulis, S.L., Deditius, A., Palacios, C., Zúñiga, A., Weldt, M., Alvear, M., 2010. "Invisible" silver
 1354 and gold in supergene digenite ($Cu_{1.8}S$). Geochim. Cosmochim. Acta 74, 6157-6173.
- 1355 Renders, P.J., Seward, T.M., 1989. The adsorption of thio gold(I) complexes by amorphous As_2S_3 and Sb_2S_3 at 25 and
 1356 90°C. Geochim. Cosmochim. Acta 53, 255-267.
- 1357 Robie, R.A., Hemingway, B.S., 1995. Thermodynamic properties of minerals and related substances at 298.15 K and
 1358 1 bar (10^5 Pascals) pressure and at higher temperatures. U.S. Geol. Survey Bull. No. 2131, 461p.
- 1359 Scaini, M.J., Bancroft, G.M., Knipe, S.W., 1998. Reactions of aqueous Au^{1+} sulphide species with pyrite as a function
 1360 of pH and temperature. Amer. Miner. 83, 316-322.
- 1361 Schoonen, M.A.A., Barnes, H.L., 1991. Mechanisms of pyrite and marcasite formation from solution: III.
 1362 Hydrothermal processes. Geochim Cosmochim Acta 55, 3491-3504.
- 1363 Shvarov, Y.V., 2008. HCh: new potentialities for the thermodynamic simulation of geochemical systems offered by
 1364 Windows. Geochem. Intern. 46, 834-839.
- 1365 Shvarov, Y.V., 2015. A suite of programs, OptimA, OptimB, OptimC, and OptimS, compatible with the Unitherm
 1366 database, for deriving the thermodynamic properties of aqueous species from solubility, potentiometry and
 1367 spectroscopy measurements. Applied Geochem. 55, 17-27. Programs are available at
 1368 http://www.geol.msu.ru/deps/geochems/soft/index_e.html.
- 1369 Simon, G., Huang, H., Penner-Hahn, J.E., Kesler, S.E., Kao, L.-S., 1999. Oxidation state of gold and arsenic in gold-
 1370 bearing arsenian pyrite. Amer. Miner. 84, 1071-1079.
- 1371 Stefánsson, A., Seward, T.M., 2003. Stability of chloridogold(I) complexes in aqueous solutions from 300 to 600°C
 1372 and from 500 to 1800 bar. Geochim. Cosmochim. Acta 67, 4559-4576.
- 1373 Stromberg, J.M., Van Loon, L.L., Gordon, R., Woll, A., Feng, R., Schumann, D., Banerjee, N.R., 2019. Applications
 1374 of synchrotron X-ray techniques to orogenic gold studies; examples from the Timmins gold camp. Ore Geol.
 1375 Rev. 104, 589-602.
- 1376 Sverjensky, D.A., Harrison, B., Azzolini, D., 2014. Water in the deep Earth: The dielectric constant and the
 1377 solubilities of quartz and corundum to 60 kb and 1200 °C. Geochim. Cosmochim. Acta 129, 125-145.
- 1378 Sylvester, P.J., Cabri, L.J., Tubrett, M.N., McMahon, G., Laflamme, J.H.G., Peregoedova, A., 2005. Synthesis and
 1379 evaluation of a fused pyrrhotite standard reference material for platinum group element and gold analysis by
 1380 laser ablation-ICPMS. In: Törmänen, T.O., and Alapieti, T.T., eds., 10th International Platinum Symposium:
 1381 Oulu, Geological Survey of Finland, Extended Abstracts, p. 16-20.
- 1382 Tauson, V.L., 1999. Gold solubility in the common gold-bearing minerals: experimental evaluation and application to
 1383 pyrite. Eur. J. Mineral. 11, 937-947.
- 1384 Tauson, V.L., Lipko, S.V., Smagunov, N.V., Kravtsova, R.G., 2018. Trace element partitioning dualism under
 1385 mineral-fluid interaction: Origin and geochemical significance. Minerals 8, 282.
- 1386 Testemale, D., Hazemann, J.-L., Pokrovski, G.S., Roux, J., Joly, Y., Argoud, R., Geaymond, O., 2004. Structural and
 1387 electronic evolution of the $As(OH)_3$ molecule in high-temperature aqueous solutions: an x-ray absorption
 1388 investigation. J. Chem. Phys. 121, 8973-8982.

- 1389 Trigub, A.L., Tagirov, B.R., Kvashnina, K.O., Chareev, D.A., Nickolsky, M.S., Shiryaev, A.A., Baranova, N.N.,
1390 Kovalchuk, E.V., Mokhov, A.V., 2017. X-ray spectroscopy study of the chemical state of “invisible” Au in
1391 synthetic minerals in the Fe-As-S system. *Amer. Miner.* 102, 1057-1065.
- 1392 Trigub, A.L., Tagirov, B.R., Kvashnina, K.O., Lafuerza, S., Filimonova, O.N., Nickolsky, M.S., 2017. Experimental
1393 determination of gold speciation in sulfide-rich hydrothermal fluids under a wide range of redox conditions.
1394 *Chem. Geol.* 471, 52-64.
- 1395 Velásquez, G., Béziat, D., Salvi, S., Siebenaller, L., Borisova, A.Y., Pokrovski, G.S., de Parseval, P., 2014. Formation
1396 and deformation of pyrite and implications for gold mineralization at the El Callao mining district, Venezuela.
1397 *Econ. Geol.* 109, 457-486.
- 1398 Widler, A.M., Seward, T.M., 2002. The adsorption of gold(I) hydrosulfide complexes by iron sulphide surfaces.
1399 *Geochim. Cosmochim. Acta* 66, 383-402.
- 1400 Yang, S., Blum, N., Rahders, E., Zhang, Z., 1998. The nature of invisible gold in sulfides from the Xiangxi Au-Sb-W
1401 ore deposit in Northwestern Hunan, People’s Republic of China. *Can. Mineral.* 36, 1361-1372.
- 1402 Xia, F., Zhou, J., Brugger, J., Ngthai, Y., O’Neill, B., Putnis, A., Pring, A., 2009. Mechanism and kinetics of
1403 pseudomorphic mineral replacement reactions: a case study of the replacement of pentlandite by violarite.
1404 *Geochim. Cosmochim. Acta* 73, 1945-1969.
- 1405 Xing, Y., Brugger, J., Tomkins, A., Shvarov Y., 2019. Arsenic evolution as a tool for understanding formation of
1406 pyritic gold ores. *Geology* 47, 335-338.
- 1407

1408

1409 **Table 1.** Batch reactor experiments: initial system compositions and gold dissolved concentrations determined
 1410 from gold weight-loss and analyses of quenched fluid from runs conducted in this study at 450°C and 700 bar.

Run number	Mass of aqueous solution loaded, g	Solids loaded	Mass of Py/Po loaded, g	Initial system composition, mol/kg fluid			Δm_{Au} , mg weight loss	Au in fluid and solid, ppm weight loss	Au in quenched fluid, ppm	Au in solid ^c , ppm
				<i>K₂S₂O₃</i>	<i>HCl</i>	<i>KOH</i>				
Py1	13.639	Py, Au	1.120	0.50	0.65	-	0.7	47	<150	ND
Py2	13.460	Py, Au	1.121	0.50	0.20	-	7.3	545	440	1260
Py3	16.843	Py, Au	0.659	0.50	0.20	-	<0.5	<30	237	ND
Py4	14.264	Py, Au	1.023	0.50	-	-	22.3	1631	1664	ND
Py5	15.246	Py, Au	0.730	0.50	-	0.31	39.0	2559	2832	ND
Py6 ^a	8.786	Py	0.935	0.50	0.20	-	<0.5	<60	2	ND
Py7 ^b	15.266	Py, Au	1.004	-	-	-	0.5	41	135	ND
Po1	15.324	Po, Au	0.308	0.50	0.20	-	10.0	652	426	6980
Po2	12.984	Po, Au	0.309	0.49	0	0.31	24.6	1608	946	13800
<i>error</i>	± 0.010 g		± 0.005 g				± 0.5 mg	± 50 ppm	$\pm 15\%$	$\pm 20\%$

1411

1412 ^a Au-free blank run for evaluating Au contamination from the autoclave and washing solutions.

1413 ^b S-poor Au-bearing blank run in water for evaluating detection limits for Au concentration determinations.

1414 ^c Derived from the difference of Au concentrations from weight loss and quenched fluid analyses and using the masses of the loaded solution and solid phase. ND here means not detected; it is applicable to cases where this difference is negative.

1415

1416

1417

1418

1419
 1420
 1421
 1422
 1423
 1424
 1425
 1426

Table 2. Flexible-cell reactor experiments: fluid composition and gold and other element dissolved concentrations measured in sampled fluids of $K_2S_2O_3$ (-HCl-KOH- $FeCl_2$) composition at the indicated *P-T*-time conditions. Also reported are the initial aqueous solution compositions and concentrations of the compounds injected into the experimental fluid. Concentrations of major solute components are in mole per 1 kg of fluid (m); those of Au in ppm.

Run name, Sample number	Days from start	S tot	sulfide	sulfate	K	Cl	Fe	Au, ppm
CoPy1 350°C, 370 bar; 0.49 m $K_2S_2O_3$ + 0.14 m HCl								
1	1	1.00	0.31	0.40	1.00	0.13	1e-4	653
2	3	1.07	0.31	0.42	1.02	0.13	2e-5	709
3	7	0.95	0.30	0.41	0.92	0.13	2e-5	625
4	10	0.97	0.30	0.39	0.97	0.13	1e-5	556
<i>Injection of KCl (0.11m)-BaCl₂(0.090m)-FeCl₂ (0.18m)</i>								
5	14	0.26	0.0043	0.21	0.86	0.74	0.027	6
6	17	0.25	0.0050	0.20	0.88	0.74	0.023	16
7	24	0.24	<0.003	0.19	0.86	0.75	0.014	37
CoPy2 350°C, 400 bar; 0.19 m $K_2S_2O_3$ + 0.091 m KOH								
1	1	0.37	0.16	0.14	0.58	<0.02	4×10 ⁻⁵	474
2	3	0.33	0.11	0.13	ND	<0.001	5×10 ⁻⁵	403
<i>Injection of FeCl₂ (0.056 m)</i>								
3	14	0.12	<0.001	0.12	0.49	0.20	0.0022	51
4	17	0.11	<0.001	0.084	0.44	0.19	0.0014	51
CoPy3 450°C, 700 bar; 0.50 m $K_2S_2O_3$ + 0.30 m KOH								
4	16	0.71	0.40	0.32	0.79	ND	ND	1552
5	20	0.69	0.35	0.24	0.78	ND	ND	1358
6	23	0.75	ND	ND	0.93	ND	ND	1365
7	27	0.59	0.37	0.28	0.60	ND	ND	1299
<i>Injection of HCl (0.172 m)</i>								
8	29	0.62	0.20	0.35	0.74	0.20	ND	561
9	32	0.57	0.19	0.31	0.68	0.18	ND	638
10	35	0.54	0.25	0.32	0.61	0.22	ND	563
<i>Injection of FeCl₂ (0.051 m)</i>								
11	37	0.43	0.13	0.33	0.68	0.27	ND	148
12	41	0.47	0.11	0.28	0.76	0.29	ND	49
13	44	0.48	0.084	0.30	0.75	0.28	ND	75
<i>Error</i>		±10%	±10%	±10%	±10%	±10%	±50%	±10%

1427
 1428
 1429

ND = not determined.

1430
1431
1432
1433

Table 3. Total gold, visible and invisible native gold, and invisible chemically bound gold concentrations in pyrite from hydrothermal batch-reactor and flexible-cell reactor experiments of this study obtained using different analytical methods.

Run	Acid digestion and ICP-AES; Au total, ppm	SEM; Au visible			EPMA ^a ;	LA-ICPMS ^b ;	X-ray Fluorescence; Au invisible		% Au(I) LCF XANES of Au invisible	Au(I) chemically bound in pyrite, ppm ^c
		S _{Au} , μm ²	S _{Py} , μm ²	Au ⁰ , ppm	Au invisible, ppm (Nb pts)	Au invisible, ppm (Nb pts)	Δμ _n ×10 ⁴	Au invisible, ppm		
Py1	100	2.7	68017	150	180 (30)	ND	0.531	52	95	50
Py2	117	3.2	57915	210	180 (21)	81 (9)	0.598	59	>97	58
Py3	ND	ND	ND	ND	ND	ND	0.552	48	88	42
Py4	605	3.2	60696	201	180 (29)	ND	4.81	471	30	141
Py5	486	51	307653	639	190 (27)	180 (8)	2.08	204	>97	204
Po1	5591	470	82194	23941	ND	320 (9)	13.73	1190	4.5	54
Po2	20418	410	89092	19286	ND	ND	16.25	1593	7.3	116
CoPy1	ND	ND	ND	ND	4000 (20)	ND	36.57	3586	46	1664
CoPy2	ND	ND	ND	ND	5000 (45)	ND	129.7	12716	5	636
CoPy3	ND	ND	ND	ND	ND	6047 (5)	132.2	12957	<3	<390
Error	±5%			±50%	±50%	±50%	±15%	±20%	±3%	±25%

1434
1435
1436
1437
1438

^a EPMA detection limit is 120 ppm Au; ^b LA-ICPMS typical detection limit is 0.1 ppm Au

^c obtained as the product of Au(I) mole fraction and the total Au concentration from fluorescence spectra from equation (2); XRF detection limit is 1 ppm Au.

ND = not determined

1439

1440 **Table 4.** Adopted gold solubility and speciation in equilibrium with metallic gold and pyrite in S-rich
 1441 hydrothermal fluid, and pyrite/fluid partition coefficient for chemically bound Au(I), obtained in this
 1442 study from pyrite-fluid exchange and Au-pyrite co-precipitation experiments.

Run	Adopted Au solubility in fluid in equilibrium with gold metal and pyrite, ppm	Calculated fluid pH	Dominant Au(I) aqueous species in fluid	Au(I) chemically bound in pyrite, ppm	Partition coefficient $D_{py/fl}$ (Au(I)) ^a
Pyrite-gold exchange experiments, 450°C, 700 bar					
Py1	150	4.4	Au(HS)S ₃ ⁻	50	0.33
Py2	440	5.4	Au(HS)S ₃ ⁻	58	0.13
Py3	237	5.4	Au(HS)S ₃ ⁻	42	0.18
Py4	832	6.6	Au(HS)S ₃ ⁻ + Au(HS) ₂ ⁻	141	0.17
Py5	1394	8.0	Au(HS) ₂ ⁻ + Au-S ₂ ⁻ + other complexes	204	0.15
Po1	426	5.8	Au(HS)S ₃ ⁻	54	0.13
Po2	946	8.1	Au(HS) ₂ ⁻ + Au-S ₂ ⁻ + other complexes	116	0.12
Pyrite-gold co-precipitation experiment, 450°C, 700 bar					
CoPy3	91	6.6	Au(HS) ₂ ⁻ + Au(HS)S ₃ ⁻	<390 ^a	<4.2 ^b
Pyrite-gold co-precipitation experiments, 350°C, 400 bar					
CoPy1	37	4.5	Au(HS)S ₃ ⁻	1664	45.0
CoPy2	51	7.4	Au(HS) ₂ ⁻	636	12.5
<i>Error</i>	±20%	±0.2 unit		±25%	±30%

1443 ^a equation (4)

1444 ^b maximum value, since Au(I) in pyrite was below detection limit in this experiment

1445

Figure captions

1446

1447

1448 **Fig. 1.** Schematic illustration of the experimental design and procedures used in this study.

1449

1450 **Fig. 2.** Scanning Electron Microscopy (SEM) microphotographs in back scattered electron (BSE) mode of
 1451 representative pyrite samples from hydrothermal experiments in the presence of dissolved gold (see Table 1
 1452 and 2) for sample identity and composition). Visible metallic gold is manifested by microscopic bright
 1453 particles associated with grey grains of pyrite of variable size and morphology. (A) Pyrite (grey) with rests
 1454 of initial pyrrhotite (light grey) and visible native gold grains (white) from acidic solution (run Po1). (B)
 1455 Pyrite and native gold from an alkaline solution (Py5). (C) and (D) Pyrites with no visible native gold, from
 1456 neutral (Py4) and acidic (Py2) solutions, respectively. (E) and (F) Pyrite powder and polished section,
 1457 respectively, from co-precipitation experiments (CoPy2 and CoPy3) with metallic gold particles of variable
 1458 size, from <0.1 to ~ 2 μm .

1459

1460 **Fig. 3.** Comparison of Au L_3 -edge XANES spectra of representative gold-bearing compounds recorded in
 1461 nominal resolution (dotted line) versus high-resolution HERFD (solid line) mode. Note that the nominal-
 1462 resolution spectra for most Au(0) and Au(I) compounds are rather featureless with weak white line
 1463 intensities and poorly resolved after-edge resonances. In contrast, spectacular improvement in spectral
 1464 resolution is apparent in HERFD mode, with each spectral feature neatly emphasized, which allows
 1465 unambiguous comparisons among samples and quantitative analyses of the different Au states in samples
 1466 with multiple Au chemical environment (e.g., using LCF).

1467

1468 **Fig. 4.** Normalized Au L_3 -edge HERFD XANES spectra of experimental pyrite samples and selected
 1469 reference compounds. The major distinguishing features of Au(0), Au(I) and Au(III) spectra are indicated
 1470 by vertical dotted lines. Pyrite spectra are grouped according to the dominant Au state: Au(0) (Po1,2, Py4,
 1471 Copy2, CoPy3 - not shown), Au(I) (Py1, 2, 3, 5), and both Au(0) and Au(I) (CoPy1). All spectra have the
 1472 same Y-axis scale, but are shifted vertically for clarity. 'Au bulk' corresponds to metallic gold of particle
 1473 size ~ 1 μm ; 'Au NP 5nm' denotes gold nanoparticles of 5 nm diameter stabilized in phosphate saline
 1474 solution.

1475

1476 **Fig. 5.** Normalized Au L_3 -edge HERFD XANES spectra of a representative experimental sample with
 1477 dominantly chemically bound Au (Py2) and its comparison with FDMNES simulated spectra of (A)
 1478 representative Au substitution models in the pyrite structure for Fe and S sites pictured by AuS_6 and
 1479 AuFe_3S clusters; (B) simple 2-, 4- and 6-coordinated AuS_n clusters of the indicated geometry, and (C)
 1480 major Au-S aqueous complexes simulated using molecular dynamics with pictured structures of the
 1481 $\text{Au}(\text{HS})\text{S}_3^-$ and $\text{Au}(\text{HS})_2^-$ species (from Pokrovski et al., 2015). It can be seen that none of Au substitution
 1482 models in pyrite crystallographic sites (Fe and S) can account for the experimental spectra, which are best
 1483 matched by S-Au(I)- S_3 clusters in which gold is linearly coordinated to 2 sulfur atoms at 2.30 \AA in the
 1484 nearest atomic shell. Vertical dashed lines in (C) indicate the energy shifts between the calculated spectra
 1485 of different Au species (see section 3.4 for detailed discussion).

1486

1487 **Fig. 6.** Distribution of major aqueous sulfur species calculated at 450°C and 700 bar as a function of pH
 1488 (controlled by addition of HCl or KOH) in a 0.5 m $\text{K}_2\text{S}_2\text{O}_3$ aqueous solution in equilibrium with pyrite.
 1489 Thermodynamic properties of the solid phases and aqueous species are from sources reported in Table A1.
 1490 Concentrations of other, minor, S species such as traditional polysulfides ($\text{S}_{n-1}\text{S}^{2-}$), thiosulfate and other
 1491 oxysulfur forms are less than 0.001 m of total S at these conditions. ' $\Sigma(\text{H})\text{SO}_4$ ' stands for the sum of the
 1492 sulfate and hydrogensulfate ions and their ion pairs with K^+ ; ' HS^- ' stands for the sum of HS^- ion and its
 1493 KHS^0 ion pair (see Table A1 for the full list of species). The small increase of the $\Sigma(\text{H})\text{SO}_4$ and HS^-
 1494 concentrations at the most alkaline pH is due to minor breakdown of pyrite to pyrrhotite. Neutral pH value
 1495 is 6.05 as defined by the dissociation constant of water ($\text{H}_2\text{O}=\text{H}^+ + \text{OH}^-$) at these P - T conditions (indicated
 1496 by the vertical dotted line).

1497

1498 **Fig. 7.** Solubility of gold at 450°C and 700 bar in a 0.5 m K₂S₂O₃ aqueous solution as a function of pH
 1499 (controlled by addition of HCl or KOH) measured in this study in batch (Py1 to 5, squares) and flexible-
 1500 cell (CoPy3, circles) reactors and its comparison with different speciation models. Model 1 (solid red
 1501 curve) includes both Au(HS)₂⁻ (Pokrovski et al., 2014) and Au(HS)S₃⁻ (Pokrovski et al., 2015) complexes.
 1502 Model 2 considers Au(HS)₂⁻ alone from Pokrovski et al. (2014), based on experimental studies in reduced
 1503 H₂S-dominated but S₃⁻-poor solutions. Model 3 considers in addition to the model 1 complexes, a disulfur
 1504 ion complex, Au(HS)S₂⁻, whose stability constant was adjusted to match the measured solubility at pH 8.
 1505 For comparison, model 3bis shows the concentration of the same Au(HS)S₂⁻ complex calculated assuming
 1506 that the exchange reaction (3) constant between HS⁻ and S₂⁻ is equal to 1, by analogy with Au(HS)S₃⁻
 1507 (Pokrovski et al., 2015). Model 4 considers Au(HS)₂⁻ alone, according to recent measurements (Trigub et
 1508 al., 2017) in concentrated S(-NaOH) solutions using similar batch reactor technique and a simplistic S
 1509 speciation model that ignores ion pairs and the sulfur radical ions and their complexes with Au.

1511 **Fig. 8.** Concentration of invisible chemically bound gold in pyrite as a function of equilibrium
 1512 concentration of gold dissolved in the fluid phase for the three types of experiments conducted in this study
 1513 (symbols). Dotted line is a linear fit through origin (on linear scale) of the 450°C and 700 bar data (Py and
 1514 Po samples), yielding an average pyrite-fluid Au(I) partitioning coefficient ($D_{py/fl}$) of 0.15±0.07. Note that
 1515 D values for the two co-precipitation experiments at 350°C (CoPy 1 and 2) are much higher ($D_{py/fl}$ between
 1516 10 and 50), while that for the 450°C co-precipitation run (CoPy3) is ~4±3 (its large uncertainty is due to the
 1517 close-to-detection-limit Au(I) fraction in pyrite from this experiment).

1518 **Fig. 9.** Schematic diagram of gold uptake and incorporation in arsenian pyrite, as a function of arsenic
 1519 content in the mineral. The dotted curve shows gold solubility limit in chemically bound state in pyrite
 1520 according to Reich et al. (2005), recalculated to mass concentration units as Au(ppm) =
 1521 526×As(wt%)+2.0. Pyrite surface is schematically shown by FeS₆ octahedrons. Gold uptake by As-
 1522 poor pyrite (<0.01 wt% As) occurs via a chemisorption step as Au-S_n complexes similar to those in S-
 1523 bearing hydrothermal fluids and their further incorporation in defects and dislocations of the growing
 1524 pyrite structure. In contrast, in presence of higher As tenors in pyrite (>0.01 wt% As), there is likely a
 1525 significant change in Au incorporation control due to arsenic, leading to large enhancement of Au
 1526 chemisorption and/or isomorphic substitution in the arsenian pyrite structure.

1528
1529

Figure captions

- 1
- 2
- 3 **Fig. 1.** Schematic illustration of the experimental design and procedures used in this study.
- 4
- 5 **Fig. 2.** Scanning Electron Microscopy (SEM) microphotographs in back scattered electron (BSE) mode of
6 representative pyrite samples from hydrothermal experiments in the presence of dissolved gold (see Table 1
7 and 2) for sample identity and composition). Visible metallic gold is manifested by microscopic bright
8 particles associated with grey grains of pyrite of variable size and morphology. (A) Pyrite (grey) with rests
9 of initial pyrrhotite (light grey) and visible native gold grains (white) from acidic solution (run Po1). (B)
10 Pyrite and native gold from an alkaline solution (Py5). (C) and (D) Pyrites with no visible native gold, from
11 neutral (Py4) and acidic (Py2) solutions, respectively. (E) and (F) Pyrite powder and polished section,
12 respectively, from co-precipitation experiments (CoPy2 and CoPy3) with metallic gold particles of variable
13 size, from <0.1 to ~2 μm .
- 14
- 15 **Fig. 3.** Comparison of Au L₃-edge XANES spectra of representative gold-bearing compounds recorded in
16 nominal resolution (dotted line) versus high-resolution HERFD (solid line) mode. Note that the nominal-
17 resolution spectra for most Au(0) and Au(I) compounds are rather featureless with weak white line intensities
18 and poorly resolved after-edge resonances. In contrast, spectacular improvement in spectral resolution is
19 apparent in HERFD mode, with each spectral feature neatly emphasized, which allows unambiguous
20 comparisons among samples and quantitative analyses of the different Au states in samples with multiple Au
21 chemical environment (e.g., using LCF).
- 22
- 23 **Fig. 4.** Normalized Au L₃-edge HERFD XANES spectra of experimental pyrite samples and selected
24 reference compounds. The major distinguishing features of Au(0), Au(I) and Au(III) spectra are indicated by
25 vertical dotted lines. Pyrite spectra are grouped according to the dominant Au state: Au(0) (Po1,2, Py4,
26 Copy2, CoPy3 - not shown), Au(I) (Py1, 2 ,3, 5), and both Au(0) and Au(I) (CoPy1). All spectra have the
27 same Y-axis scale, but are shifted vertically for clarity. 'Au bulk' corresponds to metallic gold of particle
28 size ~1 μm ; 'Au NP 5nm' denotes gold nanoparticles of 5 nm diameter stabilized in phosphate saline solution.
- 29
- 30 **Fig. 5.** Normalized Au L₃-edge HERFD XANES spectra of a representative experimental sample with
31 dominantly chemically bound Au (Py2) and its comparison with FDMNES simulated spectra of (A)
32 representative Au substitution models in the pyrite structure for Fe and S sites pictured by AuS₆ and AuFe₃S
33 clusters; (B) simple 2-, 4- and 6-coordinated AuS_n clusters of the indicated geometry, and (C) major Au-S
34 aqueous complexes simulated using molecular dynamics with pictured structures of the Au(HS)S₃⁻ and
35 Au(HS)₂⁻ species (from Pokrovski et al., 2015). It can be seen that none of Au substitution models in pyrite
36 crystallographic sites (Fe and S) can account for the experimental spectra, which are best matched by S-

37 Au(I)-S₃ clusters in which gold is linearly coordinated to 2 sulfur atoms at 2.30 Å in the nearest atomic shell.
 38 Vertical dashed lines in (C) indicate the energy shifts between the calculated spectra of different Au species
 39 (see section 3.4 for detailed discussion).

40
 41 **Fig. 6.** Distribution of major aqueous sulfur species calculated at 450°C and 700 bar as a function of pH
 42 (controlled by addition of HCl or KOH) in a 0.5 m K₂S₂O₃ aqueous solution in equilibrium with pyrite.
 43 Thermodynamic properties of the solid phases and aqueous species are from sources reported in Table A1.
 44 Concentrations of other, minor, S species such as traditional polysulfides (S_{n-1}S²⁻), thiosulfate and other
 45 oxysulfur forms are less than 0.001 m of total S at these conditions. ‘Σ(H)SO₄’ stands for the sum of the
 46 sulfate and hydrogensulfate ions and their ion pairs with K⁺; ‘HS⁻’ stands for the sum of HS⁻ ion and its KHS⁰
 47 ion pair (see Table A1 for the full list of species). The small increase of the Σ(H)SO₄ and HS⁻ concentrations
 48 at the most alkaline pH is due to minor breakdown of pyrite to pyrrhotite. Neutral pH value is 6.05 as defined
 49 by the dissociation constant of water (H₂O=H⁺ + OH⁻) at these *P-T* conditions (indicated by the vertical dotted
 50 line).

51
 52 **Fig. 7.** Solubility of gold at 450°C and 700 bar in a 0.5 m K₂S₂O₃ aqueous solution as a function of pH
 53 (controlled by addition of HCl or KOH) measured in this study in batch (Py1 to 5, squares) and flexible-cell
 54 (CoPy3, circles) reactors and its comparison with different speciation models. Model 1 (solid red curve)
 55 includes both Au(HS)₂⁻ (Pokrovski et al., 2014) and Au(HS)S₃⁻ (Pokrovski et al., 2015) complexes. Model 2
 56 considers Au(HS)₂⁻ alone from Pokrovski et al. (2014), based on experimental studies in reduced H₂S-
 57 dominated but S₃⁻-poor solutions. Model 3 considers in addition to the model 1 complexes, a disulfur ion
 58 complex, Au(HS)S₂⁻, whose stability constant was adjusted to match the measured solubility at pH 8. For
 59 comparison, model 3bis shows the concentration of the same Au(HS)S₂⁻ complex calculated assuming that
 60 the exchange reaction (3) constant between HS⁻ and S₂⁻ is equal to 1, by analogy with Au(HS)S₃⁻ (Pokrovski
 61 et al., 2015). Model 4 considers Au(HS)₂⁻ alone, according to recent measurements (Trigub et al., 2017) in
 62 concentrated S(-NaOH) solutions using similar batch reactor technique and a simplistic S speciation model
 63 that ignores ion pairs and the sulfur radical ions and their complexes with Au.

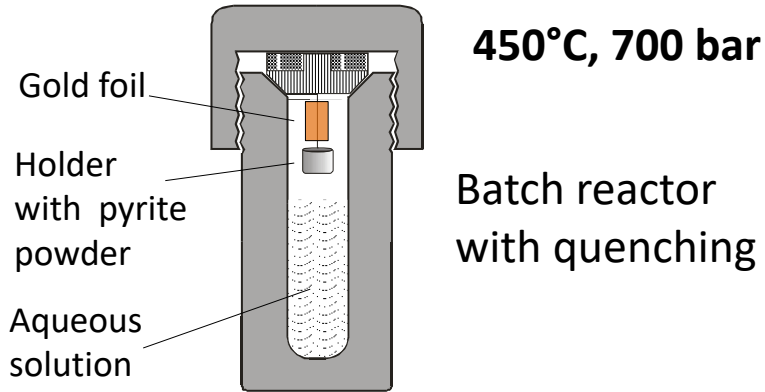
64
 65 **Fig. 8.** Concentration of invisible chemically bound gold in pyrite as a function of equilibrium concentration
 66 of gold dissolved in the fluid phase for the three types of experiments conducted in this study (symbols).
 67 Dotted line is a linear fit through origin (on linear scale) of the 450°C and 700 bar data (Py and Po samples),
 68 yielding an average pyrite-fluid Au(I) partitioning coefficient (*D_{py/fl}*) of 0.15±0.07. Note that *D* values for the
 69 two co-precipitation experiments at 350°C (CoPy 1 and 2) are much higher (*D_{py/fl}* between 10 and 50), while
 70 that for the 450°C co-precipitation run (CoPy3) is ~4±3 (its large uncertainty is due to the close-to-detection-
 71 limit Au(I) fraction in pyrite from this experiment).

72

73 **Fig. 9.** Schematic diagram of gold uptake and incorporation in arsenian pyrite, as a function of arsenic
74 content in the mineral. The dotted curve shows gold solubility limit in chemically bound state in pyrite
75 according to Reich et al. (2005), recalculated to mass concentration units as $Au(\text{ppm}) =$
76 $526 \times As(\text{wt}\%) + 2.0$. Pyrite surface is schematically shown by FeS_6 octahedrons. Gold uptake by As-poor
77 pyrite ($<0.01 \text{ wt}\% \text{ As}$) occurs via a chemisorption step as $Au-S_n$ complexes similar to those in S-bearing
78 hydrothermal fluids and their further incorporation in defects and dislocations of the growing pyrite
79 structure. In contrast, in presence of higher As tenors in pyrite ($>0.01 \text{ wt}\% \text{ As}$), there is likely a
80 significant change in Au incorporation control due to arsenic, leading to large enhancement of Au
81 chemisorption and/or isomorphic substitution in the arsenian pyrite structure.

82

Fluid-pyrite exchange of gold



Reactor quenching upon run termination



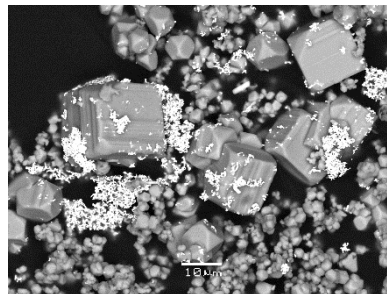
Au analysis of washout solution



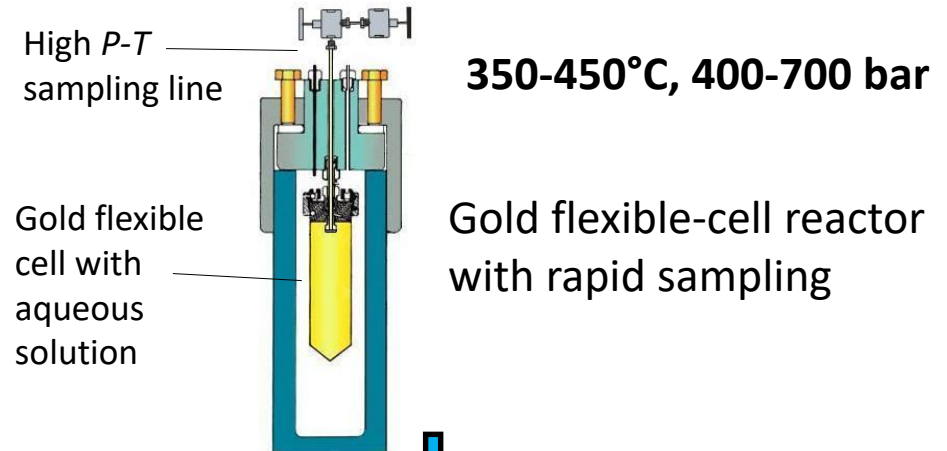
Gold foil weight loss



Pyrite analyses



Gold-pyrite co-precipitation



Fluid sampling, metal and sulfur analyses



FeCl₂ injection to induce pyrite precipitation



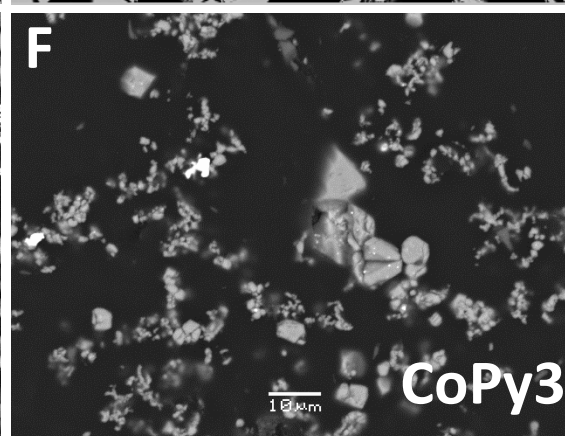
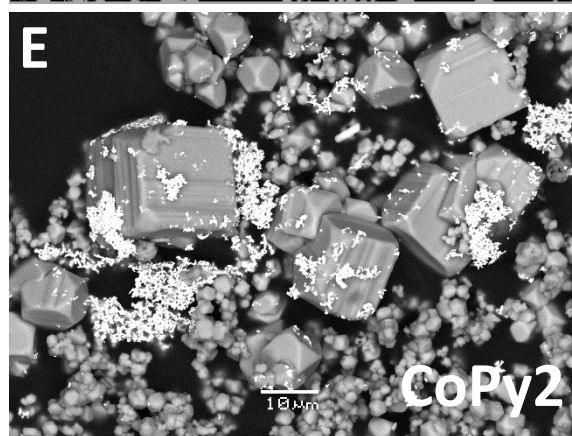
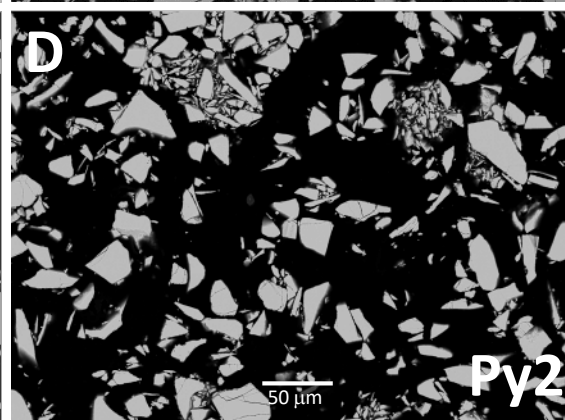
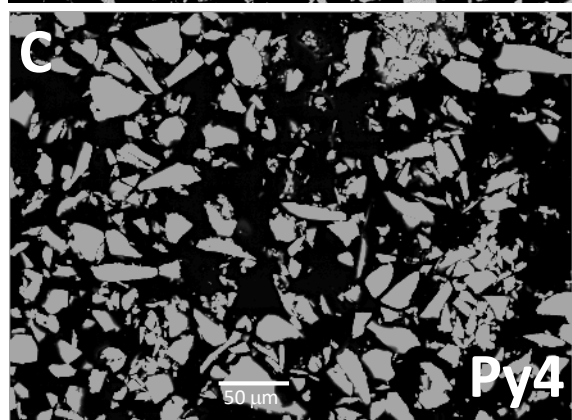
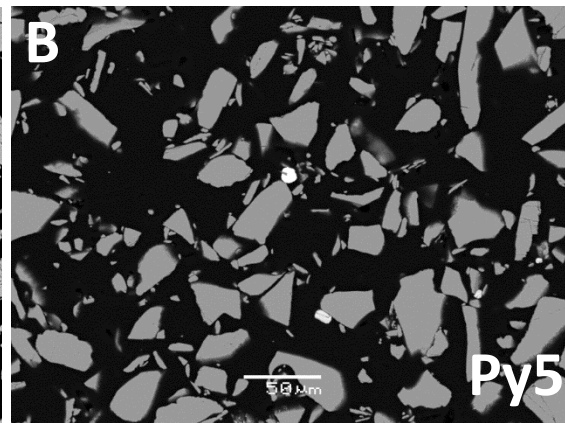
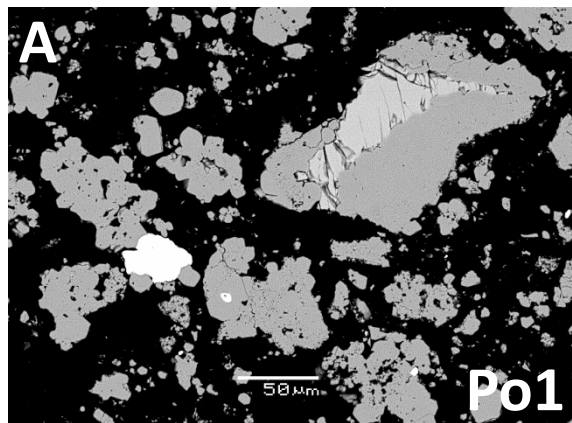
Fluid sampling, metal and sulfur analyses

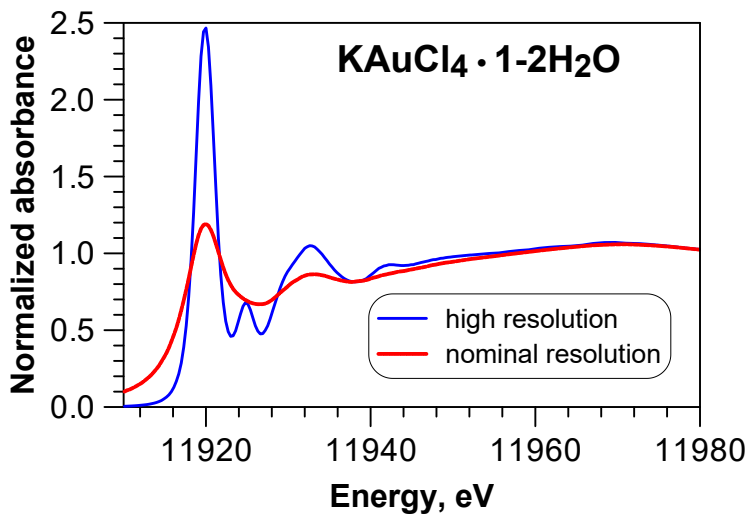
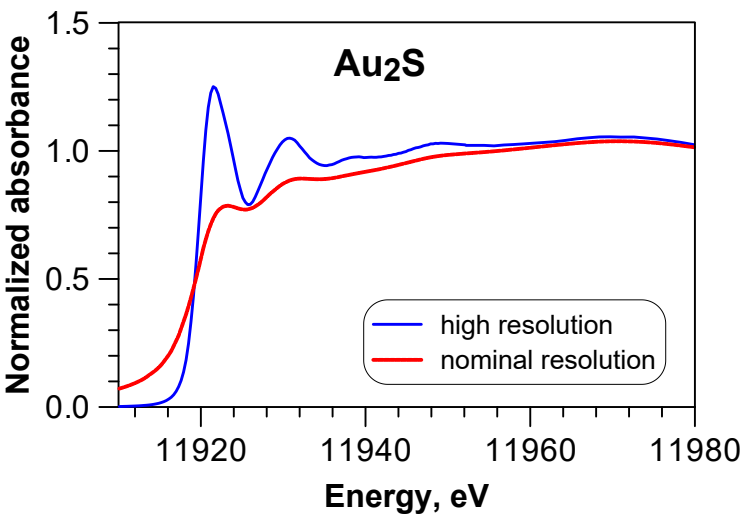
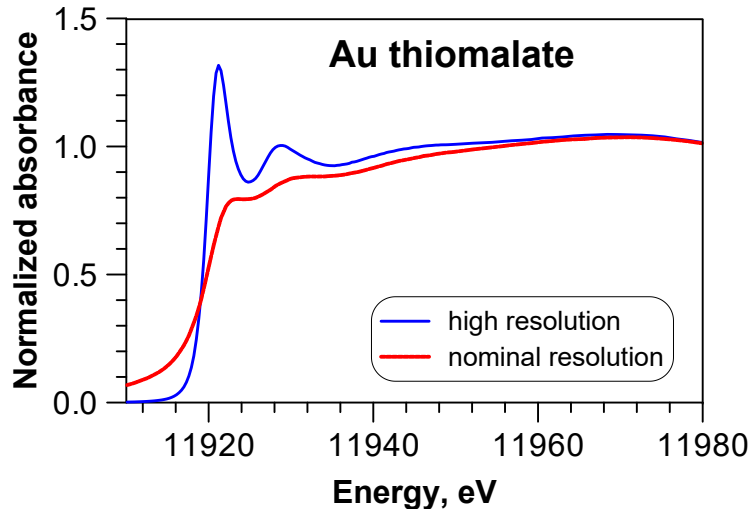
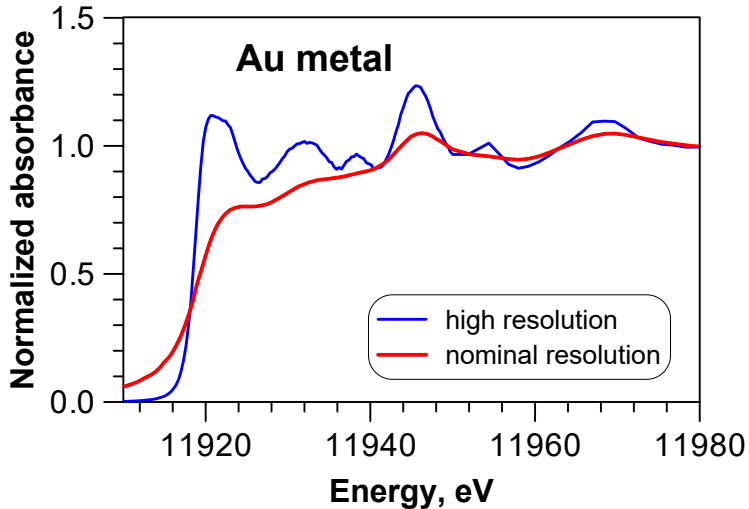


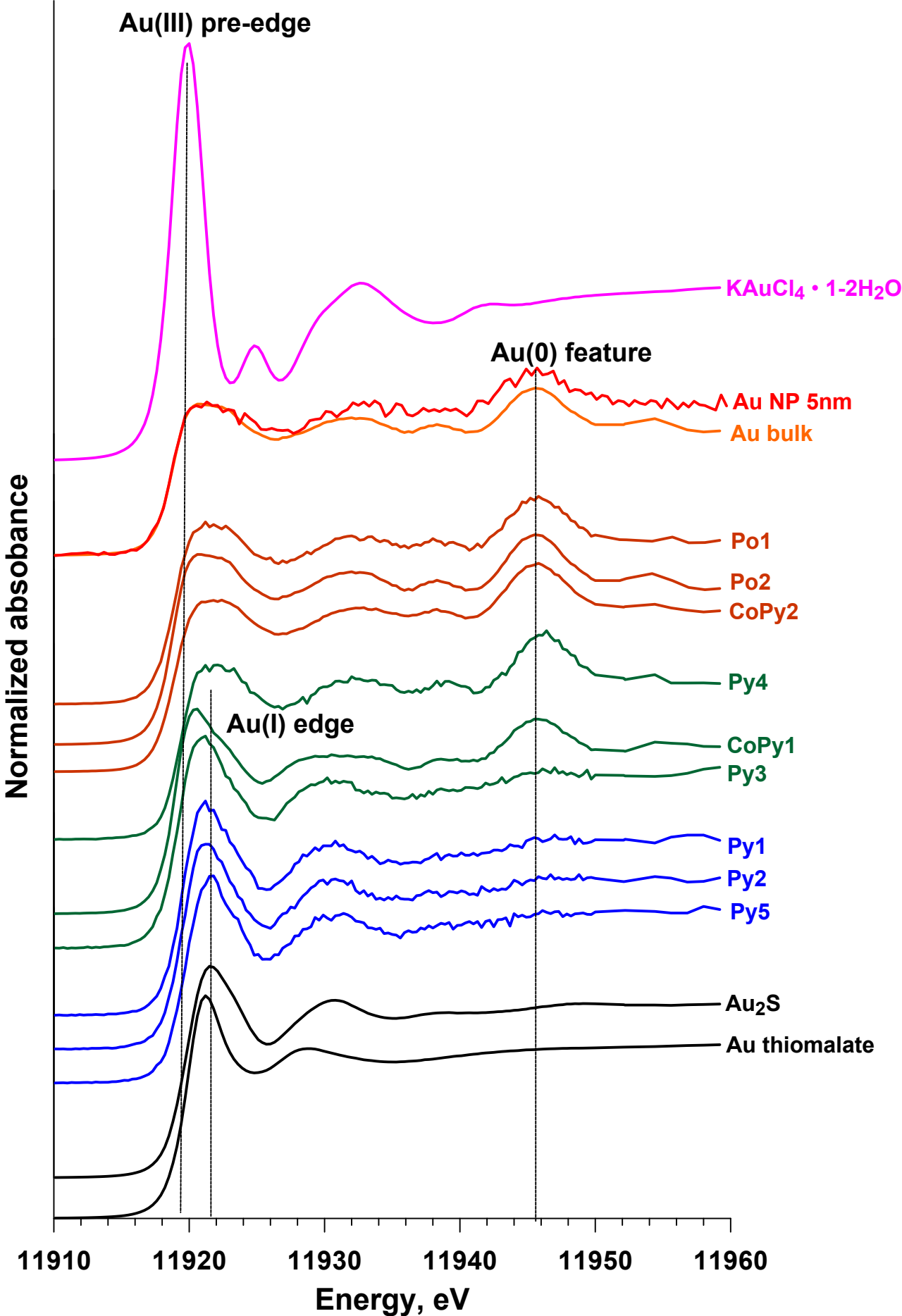
Reactor cooling

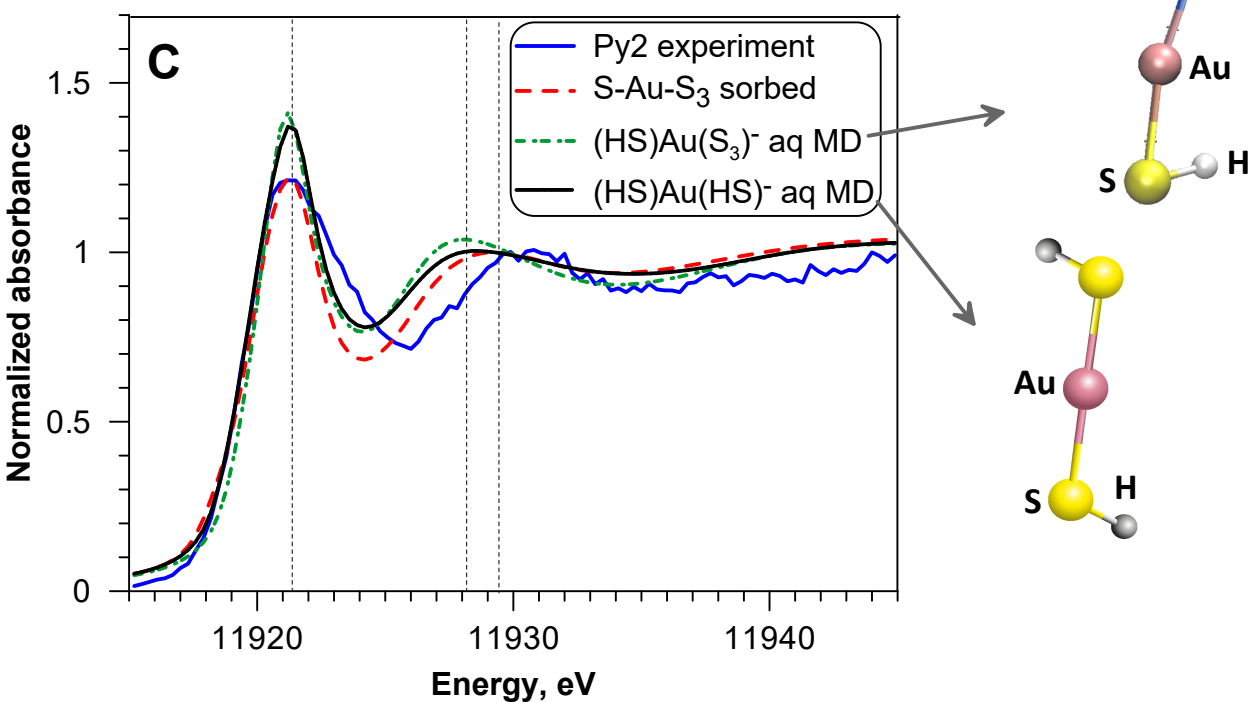
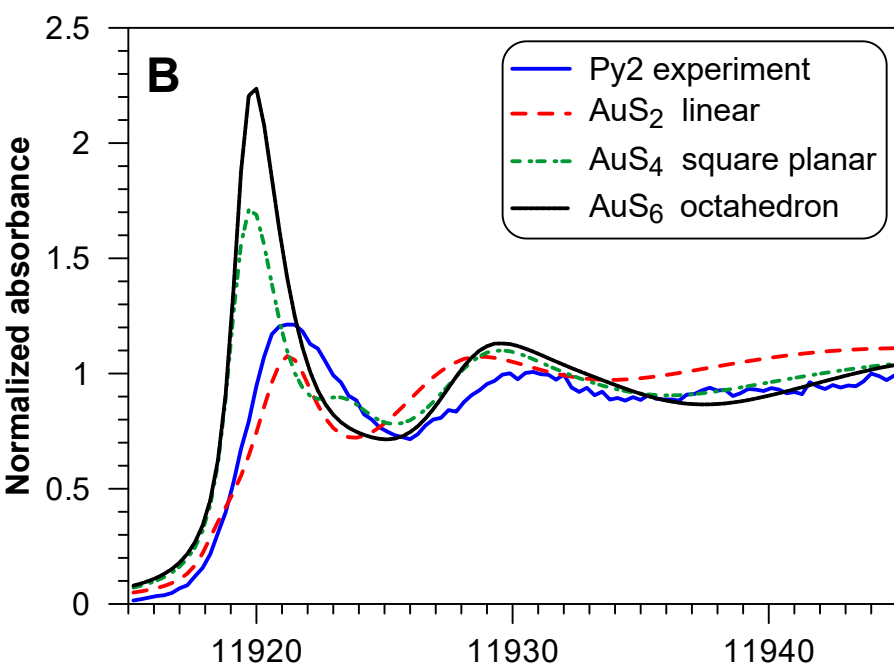
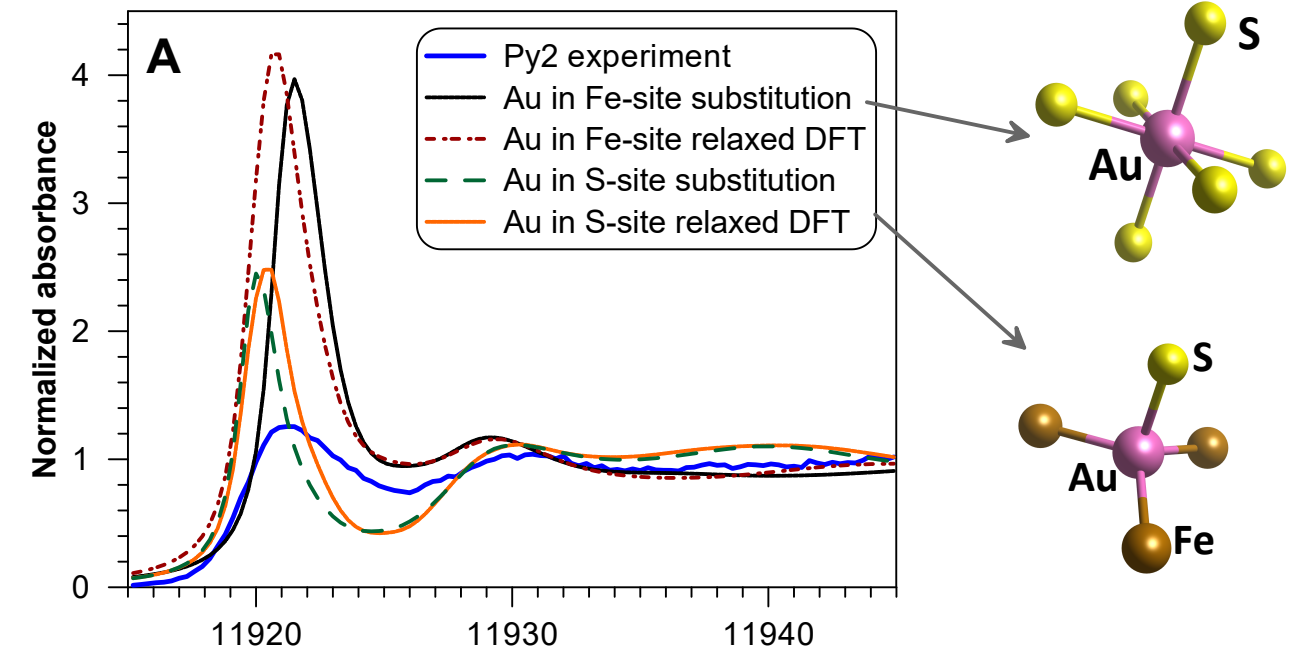


Pyrite analyses

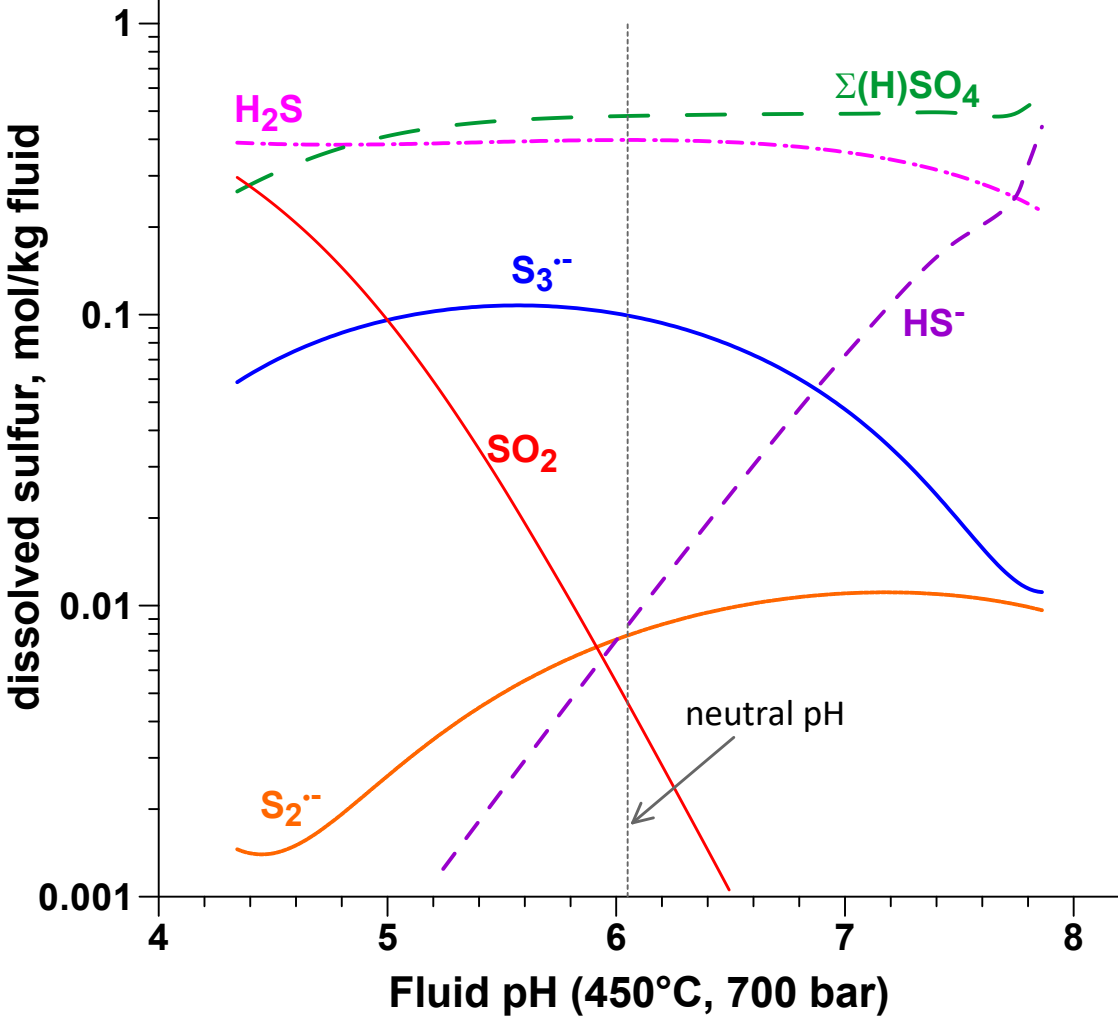


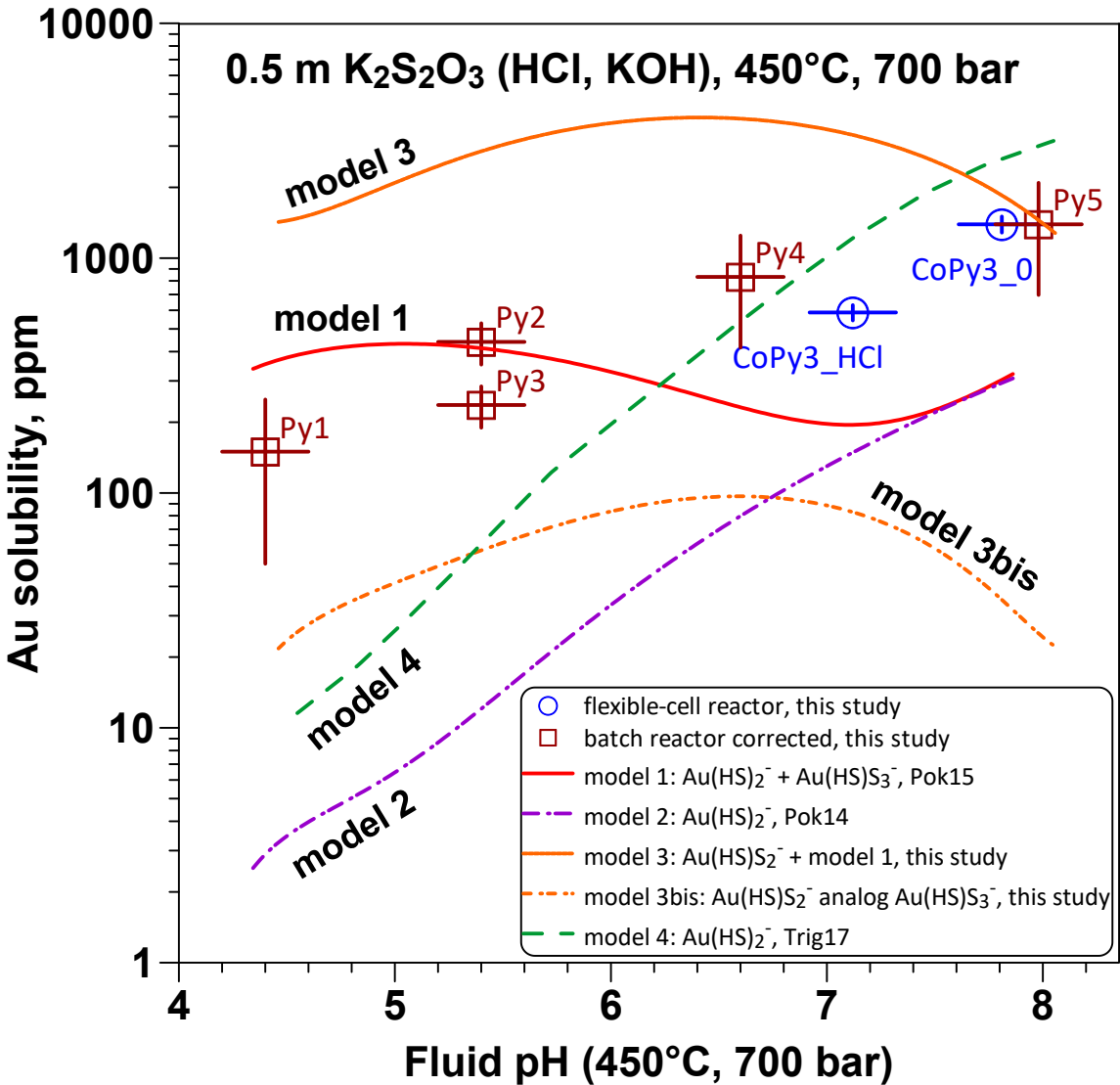


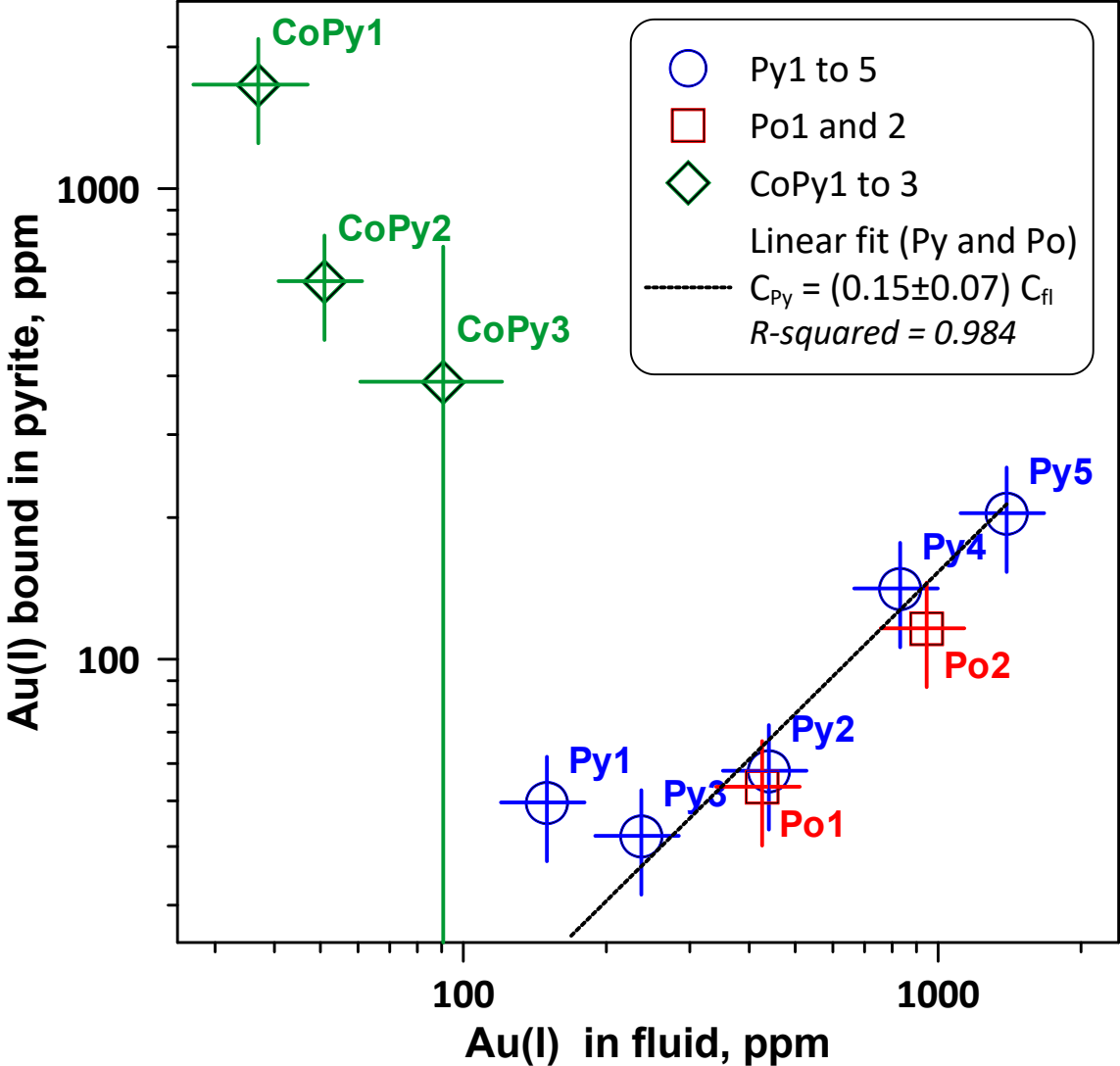


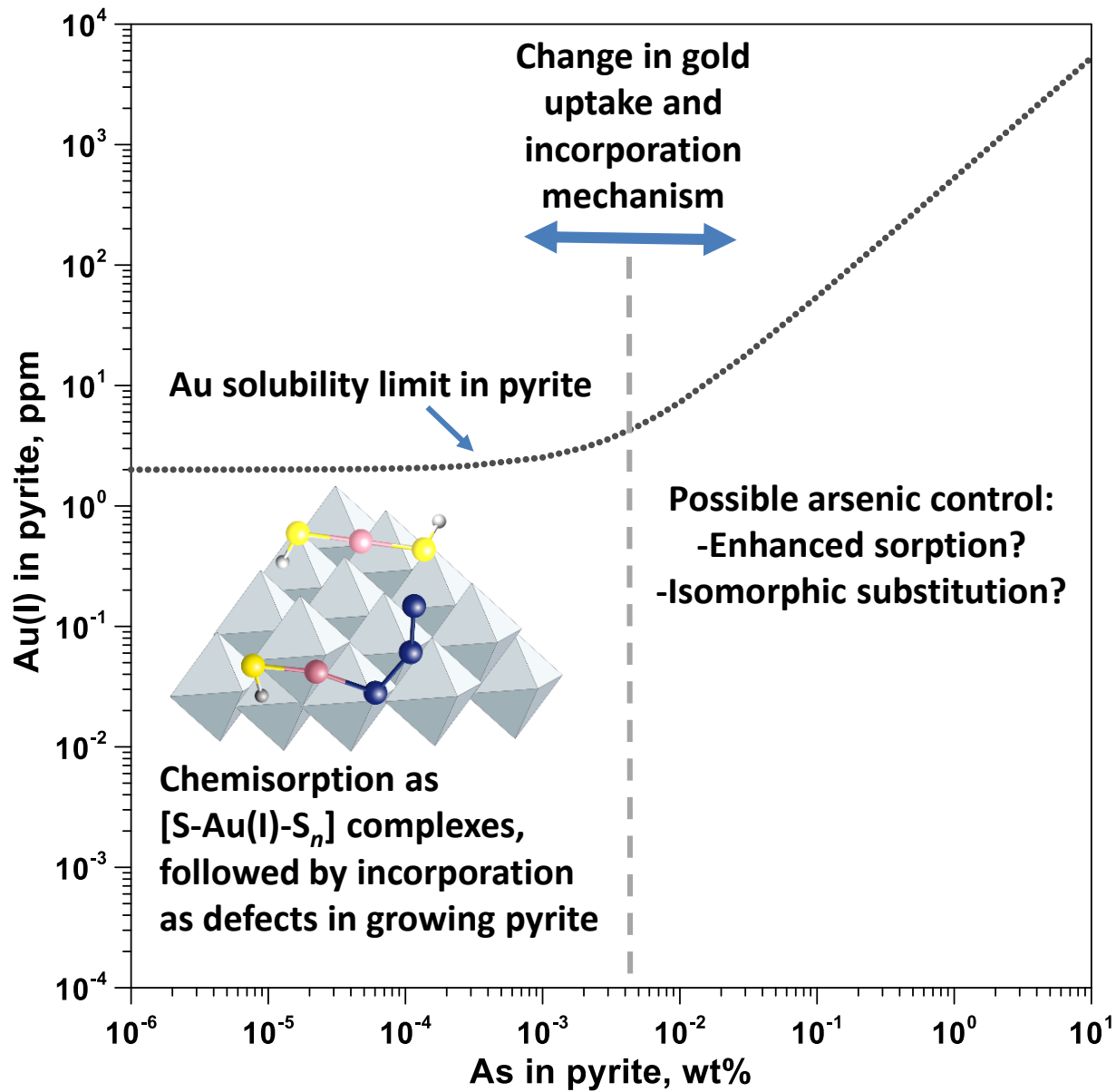


0.5 m $\text{K}_2\text{S}_2\text{O}_3$ (HCl, KOH), 450°C, 700 bar









Absorbance

